DIPLOMARBEIT

Fine Structure and Site Specific Energy Loss Spectra of NiO

Ausgeführt am Institut für
Festkörperphysik
der Technischen Universität Wien

unter der Anleitung von
Ao.Univ.Prof. Dr. Peter Schattschneider

durch
Walid Hetaba
Rechte Bahnzeile 16
3494 Gedersdorf

Wien, Mai 2011

Gottes ist der Orient!
Gottes ist der Occident!
Nord- und südliches Gelände
Ruht im Frieden seiner Hände.

Er der einzige Gerechte
Will für jedermann das Rechte.
Sey, von seinen hundert Namen,
Dieser hochgelobet! Amen.

Mich verwirren will das Irren;
doch du weißt mich zu entwirren.
Wenn ich handle, wenn ich dichte,
Gieb du meinem Weg die Richte.

Ob ich Ird'sches denk' und sinne
Das gereicht zu höherem Gewinne.
Mit dem Staube nicht der Geist zerstoben
Dringet, in sich selbst gedrängt, nach oben.

Im Atemholen sind zweyerley Gnaden:
Die Luft einziehn, sich ihrer entladen.
Jenes bedrängt, dieses erfrischt;
So wunderbar ist das Leben gemischt.
Du danke Gott, wenn er dich preßt,
Und dank' ihm, wenn er dich wieder entläßt.

Johann Wolfgang von Goethe

Zusammenfassung

Mittels des Simulationsprogramms WIEN2k wurden Berechnungen der elektronischen Struktur von NiO durchgeführt. Die mit verschiedenen Austausch-Korrelationsfunktionalen erhaltenen Ergebnisse wurden mit experimentellen Daten verglichen. Man sieht, dass das modifizierte Becke-Johnson Austauschpotential die beste Wahl für das Übergangsmetalloxid NiO ist.

Weiters wurde die Wechselwirkung zwischen dem Elektronenstrahl und der Probe mittels Energieverlust von kanalisierten Elektronen untersucht. Die Berechnungen, durchgeführt mit einem Simulationsprogramm basierend auf dem Blochwellenformalismus und dem gemischten dynamischen Formfaktor, wurden mit Experimenten verglichen und zeigen sehr gute Übereinstimmung.

Zusammenfassend kann gesagt werden, dass es die jüngsten Fortschritte bei Simulationsprogrammen erlauben, die mit komplizierten Methoden in einer neuen Generation von korrigierten Elektronenmikroskopen erhaltenen experimentellen Daten besser zu erklären.

Abstract

Electronic structure calculations for NiO were performed using the ab-initio simulation package WIEN2k. The results obtained using different exchange-correlation functionals were compared to experimental data. It is shown that the modified Becke-Johnson exchange potential is the best choice for the transition-metal oxide NiO.

Furthermore, the probe–target interaction was investigated by means of energy loss by channelled electrons. The calculations conducted using a simulation software based on the Bloch-wave formalism and the mixed dynamic form factor were compared to experiments. It is shown that the measurements are in very good agreement with the simulations.

Thus, it is shown that recent advances in simulation software allow for explaining high precision experimental data obtained by sophisticated techniques in a new generation of corrected electron microscopes.

Danksagung

Ich bedanke mich bei Prof. Peter Schattschneider für die großartige Unterstützung und Betreuung meiner Diplomarbeit. Auch danke ich ihm für seine Geduld und dafür, dass er mich schon lange vor Beginn meiner Arbeit gefördert hat.

Ganz besonderer Dank gebührt Stefan Löffler, der mir sehr viel über inelastische Elektronenstreuung beigebracht hat und den ich immer und überall mit meinen Fragen löchern durfte. Von seinem Wissen über Mathematica, LaTeX und Linux konnte ich sehr profitieren. Vor allem in den letzten Wochen meiner Arbeit war er mir eine sehr große Hilfe.

Dank geht auch an Michael Stöger-Pollach, dessen umfangreiches Wissen über die praktische Arbeit am Elektronenmikroskop einfach unersetzlich war.

Inga Ennen, Tomasz Wojcik und den Mitarbeitern von USTEM danke ich für das angenehme Arbeitsklima.

Spezieller Dank gilt Prof. Wolfgang Neumann von der Humboldt-Universität zu Berlin, der mir die Möglichkeit gab, während meines ERASMUS-Studiums in seiner Gruppe zu arbeiten und mich in meiner Entscheidung, mich dem Gebiet der Elektronenmikroskopie zu widmen, bestärkt hat. Für die freundliche Aufnahme und die gute Zusammenarbeit danke ich der gesamten Arbeitsgruppe Kristallographie, besonders aber Anna Mogilatenko, Holm Kirmse und Ines Häusler.

Der Fachschaft Physik danke ich dafür, mir während meiner Studienzeit ein zweites Zuhause geboten zu haben. Durch die Arbeit dort habe ich sehr viel gelernt, sowohl über das Leben als auch über die Physik.

Meine Eltern, Said und Karin, haben mich immer in allem was ich tat unterstützt. Dadurch konnte ich sorgenfrei das studieren, was mich am meisten interessiert hat. Auch meine Schwester Amira hat mich, vor allem in den stressigen Zeiten meines Studiums, immer aufgemuntert. Meine Großeltern, Ilse und Gustav, haben mich ebenfalls immer wieder motiviert. Dafür danke ich euch!

Contents

Part I.

Preface

1. Introduction

A new generation of corrected transmission electron microscopes (TEM) allows experiments with unprecedented high quality and precision. Thus, one cannot get along without sophisticated simulations to understand experimental data.

In transmission electron microscopy two fields need a detailed description by simulations. The first one is the calculation of the electronic structure of the sample material. The second field is the accurate modelling of the probe–target interaction.

The calculation of the electronic structure is usually done by means of ab-initio simulations. One possibility is to use the density functional theory based program package WIEN2k [1]. The crucial point of these calculations is to describe the exchange-correlation potential as accurately as possible. This is especially important for the calculation of the electronic structure of 3d transition-metals. Due to the strongly localized 3d electrons, the common local density approximation fails. In recent years new ways to describe the exchange correlation potential have come up [2, 3].

When investigating the probe–target interaction, the combination of elastic with inelastic scattering is of current interest. According to dynamical diffraction of the probe, the thickness dependence of a measured signal depends in a complicated way on the scattering geometry. These effects can already be seen as the so-called "Pendellösung" when using the Bloch-wave formalism [4]. Even in simple TEM investigations effects can be seen [5]. Particularly for sophisticated methods like "energy loss by channelled electrons" (ELCE) [6], "atom location by channelling enhanced microanalysis" (ALCHEMI) [7] or "energy-loss magnetic chiral dichroism" (EMCD) [8], the detailed description of the probe–target interaction plays an important role, which often does not get sufficient attention.

As NiO is a 3d transition-metal oxide, it is an ideal example material to demonstrate the effect of different exchange correlation potentials and compare the results with experimentally acquired data. Furthermore, due to its easy to understand crystal structure it is a good system to study the effects of probe–target interaction by means

of ELCE. Thus, NiO is a versatile sample to analyse the agreement of state-of-the-art simulation methods with experimental measurements.

The present work is composed of four major parts. After this brief introduction, in part one a short description of the used sample with respect to magnetic behaviour, crystallography and conduction properties is given.

The second part deals with the electronic structure calculations. In chapter 3 the theoretical background of the simulation package WIEN2k is summarised. The performed calculations and the comparison with experimental data are shown in chapter 4.

Following this, in the third part the theoretical foundations of the investigation of the probe–target interaction in the ELCE technique are laid out in chapter 5. In chapter 6 the corresponding simulations are described, while in chapter 7 the measurements and the comparison with the simulations are shown.

The final part, composed of a summary and short outlook, concludes this thesis.

2. Material

NiO is an antiferromagnetic material with a Néel temperature of $T_N = 523$ K [9]. Above this temperature it is paramagnetic with a cubic crystal structure. Below T_N NiO is in an antiferromagnetic state with a slight rhombohedral distortion which arises from a contraction of the cubic unit cell along one of the $\langle 1\,1\,1 \rangle$ axes [10]. As this distortion is very small, in this work the unit cell of NiO is described as cubic with space group number 225 ($Fm\bar{3}m$) and a lattice parameter of $a = 0.417$ nm. The Nickel atoms occupy the positions $(x = 0, y = 0, z = 0)$ of the unit cell, while the Oxygen atoms are found on positions $(x = 0.5, y = 0.5, z = 0.5)$. The crystallographic data is taken from Pearson's Handbook of Crystallographic Data [11].

The atomic spins are arranged in ferromagnetic layers parallel to the $(1\,1\,1)$ plane, see [10]. The direction of the spins are alternating in adjacent layers. As the net magnetic moment cancels, no special procedure is necessary for investigating the NiO sample in the transmission electron microscope, as it would be required for a ferromagnetic material.

With Nickel as a 3d transition-metal, NiO belongs to the transition-metal oxides whose electronic structures show insulating behaviour. Two transition-metal electrons saturate the 2p-shell of Oxygen, thus leading to O^{2-} and Ni^{2+} ions [12]. But also an amount of O 2p-Ni 3d hybridization is present [12].

The width of the band gap is determined by interionic excitations between two Ni^{2+} ions where a 3d electron is transferred from one transition-metal site to another. There are two different types of such transitions [12]. For the first one, the Coulomb correlation energy U is needed to create a 3d hole at one transition-metal ion and transfer the electron to another one:

$$3d^n + 3d^n + U \rightarrow 3d^{n-1} + 3d^{n+1}\,. \tag{2.1}$$

This type is called a Mott-Hubbard transition. If the 3d hole is screened by charge

transfer from the Oxygen ligand, the charge transfer energy Δ is needed and the hole is finally located at the ligand:

$$3\mathrm{d}^{\mathrm{n}}L + 3\mathrm{d}^{\mathrm{n}}L + \Delta \rightarrow 3\mathrm{d}^{\mathrm{n}}L^{-1} + 3\mathrm{d}^{\mathrm{n+1}}L\,. \tag{2.2}$$

A material is called a Mott-Hubbard insulator if $U < \Delta$ and it is called a charge-transfer insulator if $\Delta < U$. If U and Δ are comparable, the material is an insulator of mixed type. In [13] NiO is described as an insulator of this mixed form.

The NiO sample used for investigations in the electron microscope was prepared in [1 1 0] zone axis. This was done by subsequent cutting and polishing of the crystal. Afterwards the sample was ion milled in the GATAN Precision Ion Polishing System (PIPS). Final thinning was carried out in a Technoorg Linda Gentle Mill.

Part II.

Energy Loss Near Edge Structure

3. Theoretical Background

3.1. WIEN2K

In solid state physics one usually has to deal with a number of electrons which is of the order of 10^{23}, so one ends up with a many-body Schrödinger equation which cannot be solved analytically. There are different approaches to solve such problems. A common way is the Hartree-Fock (HF) method where the wave functions of electrons are written as Slater-determinants and exchange symmetry is accounted for.

Another way is the density functional theory (DFT) which was developed in 1964 and 1965 by P. Hohenberg, W. Kohn and L. J. Sham [14, 15]. This, together with the full potential linearized augmented plane wave (FP-LAPW) method is used in the simulation package WIEN2k [1].

Many articles and books were written about DFT and how it is implemented in WIEN2k (see for example [1, 16, 17]). These works are mainly directed to people who devote the main part of their scientific work to the development of DFT codes or the work with WIEN2k. For scientists who just want to use WIEN2k in addition to their work (e.g. electron microscopists), the simulation package often seems to work like a black box. The input variables are given and some parameters are adjusted until the result looks fine. But what is done by the program and in what way the desired values are calculated is not easy to understand. Therefore, in this chapter a short introduction to WIEN2k and its theoretical background is given.

3.1.1. Density Functional Theory

In a solid with N nuclei one has to deal with $N + Z \cdot N$ particles. The many-particle Hamiltonian in real space is then

$$\begin{aligned}\hat{H} = &-\frac{\hbar^2}{2}\sum_i^N \frac{\nabla^2_{\boldsymbol{R}_i}}{M_i} - \frac{\hbar^2}{2}\sum_i^N \frac{\nabla^2_{\boldsymbol{r}_i}}{m_e} \\ &-\frac{1}{4\pi\epsilon_0}\sum_{i,j}^N \frac{e^2\, Z_i}{|\boldsymbol{R}_i - \boldsymbol{r}_j|} + \frac{1}{8\pi\epsilon_0}\sum_{i\neq j}^N \frac{e^2}{|\boldsymbol{r}_i - \boldsymbol{r}_j|} + \frac{1}{8\pi\epsilon_0}\sum_{i\neq j}^N \frac{e^2\, Z_i\, Z_j}{|\boldsymbol{R}_i - \boldsymbol{R}_j|}\,. \end{aligned} \tag{3.1}$$

Z_i is the atomic number of the atom i, M_i is the mass of the nucleus i at position R_i while the electrons with mass m_e are at positions r_i. The first two terms describe the kinetic energies of the nuclei and electrons, the last three terms describe the electron-nucleus, electron-electron and nucleus-nucleus Coulomb interaction. As the mass of the nuclei is much bigger than the electron mass the Born-Oppenheimer approximation can be used.[1] Therefore, the kinetic energy of the nuclei and the Coulomb interaction between the nuclei can be ignored for the description of the electrons. From now on, one can assume the electrons moving in an external potential caused by the nuclei of the crystal. The Hamilton operator then can be written as

$$\hat{H} = \hat{T} + \hat{V}_{ne} + \hat{V}_{ee}\,, \tag{3.2}$$

with $\hat{T}$ the kinetic energy, $\hat{V}_{ne}$ the nucleus-electron and $\hat{V}_{ee}$ the electron-electron interaction. The total energy is the sum of the eigenvalues E of $\hat{H}$ and the nucleon-nucleon interaction

$$W = E + V_{nn}\,. \tag{3.3}$$

All terms except the kinetic energy and the electron-electron interaction are summed up as the external potential V_{ext}. Now the Hamiltonian reads

$$\hat{H} = \hat{T} + \hat{V}_{ee} + \hat{V}_{ext}\,. \tag{3.4}$$

[1] The Born-Oppenheimer approximation consists of two steps. In the first one it is assumed that the total wave function can be separated into a product of a wave function of the nuclei and a wave function of the electrons in which the $\boldsymbol{R}_i$ are only parameters. In the second step the effect of $\nabla^2_{\boldsymbol{R}_i}$ on the electron wave function is neglected. This is justified by the large mass difference of electrons and nuclei.

The electron-electron interaction is further decomposed in the classical Coulomb energy (Hartree energy $\hat{V}_H$) and the quantum mechanic exchange-correlation energy $\hat{V}_{xc}$:

$$\hat{V}_{ee} = \hat{V}_H + \hat{V}_{xc}\,. \tag{3.5}$$

Density functional theory is based on the two Hohenberg-Kohn theorems [14, 15]. The first theorem states that the external potential V_{ext} is fully determined by the ground-state electron density ρ. A given many-body system with a unique external potential yields (by solving the Schrödinger equation) a unique ground-state wave function and ground-state energy. Therefore, the total energy is a functional of the ground-state density

$$\begin{aligned} E = E[\rho] &= T[\rho] + V_{ext}[\rho] + V_{ee}[\rho] \\ &= \int \rho(\boldsymbol{r})\, V_{ext}(\boldsymbol{r})\, d\boldsymbol{r} + F_{HK}[\rho]\,. \end{aligned} \tag{3.6}$$

The Hohenberg-Kohn density functional $F_{HK}[\rho] := T[\rho] + V_{ee}[\rho]$ is a universal functional for any many-body system because it is not dependent on the external potential V_{ext}.

The second Hohenberg-Kohn theorem states that the energy is minimized as a functional of the electronic density. For any trial density $\rho(\boldsymbol{r}) \geq 0$ and $\int \rho(\boldsymbol{r}) d\boldsymbol{r} = N$, with N the total number of electrons, the relation $E_0 \leq E[\rho]$ is fulfilled. This makes it possible to use the Rayleigh-Ritz variational principle to find the ground-state density. Of all possible densities the one which minimizes $E[\rho]$ is the corresponding ground-state electron density with respect to the external potential V_{ext}.

The corresponding Hamiltonian, called the Kohn-Sham Hamilton operator, is written as

$$\begin{aligned} \hat{H}_{KS} &= \hat{T} + \hat{V}_H + \hat{V}_{xc} + \hat{V}_{ext} \\ &= -\frac{\hbar^2}{2m_e} \sum_i \nabla_i^2 + \frac{e^2}{4\pi\epsilon_0} \int \frac{\rho(\boldsymbol{r}')}{|\boldsymbol{r} - \boldsymbol{r}'|} d\boldsymbol{r}' + \hat{V}_{xc} + \hat{V}_{ext}\,. \end{aligned} \tag{3.7}$$

Like $\hat{V}_H$, the exchange-correlation operator $\hat{V}_{xc}$ depends on the electronic density ρ, see [16]. It is given by the functional derivative

$$\hat{V}_{xc} = \frac{\delta V_{xc}[\rho]}{\delta \rho}\,, \tag{3.8}$$

where V_{xc} denotes the exchange-correlation energy. The corresponding total energy can then be written as

$$E[\rho] = T[\rho] + V_H[\rho] + V_{xc}[\rho] + V_{ext}[\rho]\,, \tag{3.9}$$

with the Hartree energy as

$$V_H[\rho] = \frac{e^2}{8\pi\epsilon_0} \int \frac{\rho(\boldsymbol{r})\rho(\boldsymbol{r}')}{|\boldsymbol{r} - \boldsymbol{r}'|} d\boldsymbol{r} d\boldsymbol{r}'\,. \tag{3.10}$$

The exchange-correlation energy is not known, but in a common approximation, the local density approximation (LDA), it can be written as

$$V_{xc}[\rho] = \int \rho(\boldsymbol{r})\epsilon_{xc}(\rho(\boldsymbol{r}))d\boldsymbol{r}\,, \tag{3.11}$$

where $\epsilon_{xc}(\rho(\boldsymbol{r}))$ is approximated by a local function of the electron density. In this approximation ϵ_{xc} is no longer a functional, but a function of the electron density. The electron density is given by a sum over all occupied orbitals

$$\rho(\boldsymbol{r}) = \sum_{i=1}^{N} \phi_i^*(\boldsymbol{r})\phi_i(\boldsymbol{r})\,. \tag{3.12}$$

The highest occupied orbital is determied by the electron count. The single-particle wave functions $\phi_i(\boldsymbol{r})$ are the solutions of the Kohn-Sham equation

$$\hat{H}_{KS}\phi_i(\boldsymbol{r}) = \epsilon_i\phi(\boldsymbol{r})\,, \tag{3.13}$$

with ϵ_i the corresponding Kohn-Sham eigenvalues. One has to be aware that the total Energy $E[\rho]$ evaluated for the ground-state electronic density gives the corresponding ground-state energy. One has to keep in mind that this is a ground state algorithm which is only valid for energies close to the ground state energy. Also the $\phi_i(\boldsymbol{r})$ are

not real electron wave functions and ϵ_i are not single-electron energies. Only the electronic density, evaluated using these functions, is the electronic density of the system.

For a spin-polarized system the charge density consists of a spin-up and a spin-down density

$$\rho(\boldsymbol{r}) = \rho_\uparrow(\boldsymbol{r}) + \rho_\downarrow(\boldsymbol{r}) \tag{3.14}$$

and the magnetization density reads

$$m(\boldsymbol{r}) = \rho_\uparrow(\boldsymbol{r}) - \rho_\downarrow(\boldsymbol{r})\,. \tag{3.15}$$

The ground-state energy is then a functional of both spin directions

$$E = E[\rho_\uparrow, \rho_\downarrow]\,. \tag{3.16}$$

The Kohn-Sham equation becomes now spin-polarized

$$(\hat{T}(\boldsymbol{r}) + \hat{V}_H(\boldsymbol{r}) + \hat{V}_{xc,\sigma}(\boldsymbol{r}) + \hat{V}_{ext}(\boldsymbol{r}))\phi_{i,\sigma}(\boldsymbol{r}) = \epsilon_{i,\sigma}\phi_{i,\sigma}(\boldsymbol{r})\,, \tag{3.17}$$

with σ the spin index. The spin density reads

$$\rho_\sigma(\boldsymbol{r}) = \sum_{i=1}^{N_\sigma} \phi^*_{i\sigma}(\boldsymbol{r})\phi_{i\sigma}(\boldsymbol{r})\,, \tag{3.18}$$

with the highest occupied orbital defined by the electron count again. The exchange-correlation potential becomes

$$\hat{V}_{xc,\sigma}(\boldsymbol{r}) = \frac{\delta V_{xc}[\rho_\uparrow, \rho_\downarrow]}{\delta\rho_\sigma(\boldsymbol{r})}\,. \tag{3.19}$$

Now there are two sets of equations to be solved, one for each spin-direction, and the exchange-correlation potential is the only spin-dependent operator in the Kohn-Sham equation. For WIEN2k calculations the terms “spin-up” and “spin-down” are just arbitrary labels with no additional conditions.

As the ground-state electronic density has the periodicity of the crystal-lattice, so does the Kohn-Sham Hamiltonian. Therefore, one can make use of Bloch's theorem (see also section 5.2). It states that the wave function of an electron in a periodic

potential has the same periodicity and it can be written as the product of a plane wave and a periodic function

$$\psi_{\boldsymbol{k}+\boldsymbol{G}}(\boldsymbol{r}) = \psi_{\boldsymbol{k}}(\boldsymbol{r}) = e^{i\boldsymbol{k}\boldsymbol{r}} u_{\boldsymbol{k}}(\boldsymbol{r})\,. \tag{3.20}$$

The Kohn-Sham eigenvalue problem has to be solved only at each $\boldsymbol{k}$-point on a $\boldsymbol{k}$-grid in the irreducible wedge of the Brillouin zone. As the Hartree operator $\hat{V}_H$ and the exchange-correlation operator $\hat{V}_{xc}$ depend on the electron density $\rho(\boldsymbol{r})$ which itself again depends on the single-particle wave functions, this is a self-consistency problem. It is solved iteratively by guessing a starting density ρ_0. The $\hat{V}_H$ and $\hat{V}_{xc}$ are determined and $\hat{H}_{KS}$ is constructed. The eigenvalue problem is solved, the resulting wave functions ϕ_i are used to calculate the density ρ_{out}. In order to stabilize calculations this density is mixed with the input density to find a new input density ρ_{in}. This procedure is repeated until convergence is reached. In the simulation package WIEN2k this is called self-consistent field (SCF) cycle.

3.1.2. Linearized Augmented Plane Waves

To solve the Kohn-Sham equations the linearized augmented plane wave (LAPW) method is used. This is an enhancement of the original augmented plane wave (APW) method. For a short overview of the different methods see [17]. The Kohn-Sham wave functions are expanded in the basis set of these LAPW's

$$\phi_{\boldsymbol{k}} = \sum_n c_n \phi_{\boldsymbol{k}_n}\,, \tag{3.21}$$

with

$$\boldsymbol{k}_n = \boldsymbol{k} + \boldsymbol{K}_n\,. \tag{3.22}$$

To maintain consistency with literature, a transition of the ϕ_i in equation (3.13) to $\phi_{\boldsymbol{k}}$ in equation (3.21) is done. The $\boldsymbol{K}_n$ are reciprocal lattice vectors, with n the band index as according to Bloch's theorem, different Brillouin zones represent different bands. The $\boldsymbol{k}$ are vectors inside the Brillouin zone. The unit cell is divided into muffin-tin spheres S_α and the interstitial region I. The muffin-tin spheres with the radius R^α_{MT} are centred around the atoms α. The R^α_{MT} are defined during the initialization process of WIEN2k. They have to be chosen such that all the core states are confined

within the spheres. Care has to be taken though that the spheres of different atoms do not overlap, which is checked by the program *nn* during initialization. The wave functions $\phi_{\boldsymbol{k}}$ are expanded into plane waves in the interstitial region. In the muffin-tin spheres the $\phi_{\boldsymbol{k}}$ are expanded to a basis consisting of radial solutions of the atomic Schrödinger equation and their energy derivatives:

$$\phi_{\boldsymbol{K}}^{\boldsymbol{k}}(\boldsymbol{r}) = \begin{cases} \frac{1}{V} e^{i(\boldsymbol{k}+\boldsymbol{K})\boldsymbol{r}} & \boldsymbol{r} \in I \\ \sum_{\ell,m} \left(A_{\ell m}^{\boldsymbol{k}+\boldsymbol{K}} u_\ell(r, E_{1,\ell}) + B_{\ell m}^{\boldsymbol{k}+\boldsymbol{K}} \dot{u}_\ell(r, E_{1,\ell}) \right) Y_m^\ell(\hat{\boldsymbol{r}}) & \boldsymbol{r} \in S_\alpha \end{cases} \tag{3.23}$$

with the u_ℓ defined by

$$\left[-\frac{\mathrm{d}^2}{\mathrm{d}r^2} + \frac{\ell(\ell+1)}{r^2} + V(r) - \frac{2m_e}{\hbar^2} E_{1,\ell} \right] r u_\ell(r) = 0 \tag{3.24}$$

and

$$\dot{u}_\ell(r, E) = \left. \frac{\partial u_\ell(r, E)}{\partial E} \right|_{E=E_{1,\ell}} \tag{3.25}$$

and V in the plane wave expansion is the volume of the unit cell. The index 1 of $E_{1,\ell}$ will become clear, when local orbitals are explained later on. Equations (3.24) and (3.25) are calculated numerically on a radial mesh inside the muffin-tin spheres. This mesh is determined during the initialization process.

In principal the sum in equation (3.21) is infinite. In the calculations it is limited by a value K_{max} with $K_n \leq K_{max}$. The value is given during the initialization by defining the product $R_{MT} \cdot K_{max}$, which is usually between 6.0 and 10.0. Thus, the size of the basis set of the expansion is limited. Also the value of ℓ in the expansion inside the muffin-tin sphere is limited by ℓ_{max}. For a given K_{max} it has to be chosen such that the truncation of the two functions in (3.23) match at the sphere boundary. The spherical harmonics have at most $2\ell_{max}$ nodes on a great circle. The plane waves have K_{max}/π nodes per unit length. Therefore, a reasonable criterion is $R_{MT} \cdot K_{max} = \ell_{max}$. The coefficients $A_{\ell m}^{\boldsymbol{k}+\boldsymbol{K}}$ and $B_{\ell m}^{\boldsymbol{k}+\boldsymbol{K}}$ are determined by the condition that the function inside the muffin-tin sphere has to match the plane waves in value and slope at the sphere boundary. They can be found by expanding the plane waves into spherical harmonics, see [16]. The parameter $E_{1,\ell}$ should be chosen in the centre of the corresponding valence band (e.g. s-states correspond to $\ell = 0$, p-states to $\ell = 1$, etc.). Reasonable values are usually calculated by *lstart* during the initialization. Valence states are

separated from core states by the cutoff-energy which can be chosen during the initialization of the calculation. The standard value is $-6.0\,\mathrm{Ry}$ which means that all states below this value (counted from the Fermi energy) are treated as core-state. Calculations for the core-states can be done as if they were states of free atoms in a potential caused by the valence electrons. These calculations are done during the SCF cycle in the program *lcore*. All states with energies higher than the cutoff-energy are treated as valence states. Core-states should be completely confined in the muffin-tin sphere. It can happen that core states with an energy below the cutoff-energy reach out of the sphere. These states, called semi-core states, can then be treated as *local orbitals* (LO). The local orbitals are defined as:

$$\phi_{LO}^{\ell m}(\boldsymbol{r}) = \begin{cases} 0 & \boldsymbol{r} \notin S_\alpha \\ \left(A_{\ell m}^{LO} u_\ell(r, E_{1,\ell}) + B_{\ell m}^{LO} \dot{u}_\ell(r, E_{1,\ell}) + C_{\ell m}^{LO} u_\ell(r, E_{2,\ell})\right) Y_m^\ell(\hat{\boldsymbol{r}}) & \boldsymbol{r} \in S_\alpha\,. \end{cases} \tag{3.26}$$

These functions are defined for fixed ℓ and m and show no $\boldsymbol{k}$ or $\boldsymbol{K}$ dependence. The parameter $E_{2,\ell}$ is chosen to be in the centre of the band with the same ℓ and the next lower value of the quantum number n.

All the described parameters and values are given in the file *case.in1* as the calculations of the eigenvalues and eigenvectors of the valence states are calculated by the program *lapw1* during the SCF cycle. Choosing these values carefully is crucial to get a well converged calculation with physically meaningful results.

In WIEN2k it is possible to make use of another method for the expansion of the wave functions. This method is called augmented plane waves + local orbitals (APW+lo). It is again an enhancement of the LAPW method and similar to the original APW method. The APW+lo basis set consists of two types of functions. The first are APW's at a fixed energy $E_{1,\ell}$:

$$\phi_{\boldsymbol{K}}^{\boldsymbol{k}}(\boldsymbol{r}) = \begin{cases} \frac{1}{V} e^{i(\boldsymbol{k}+\boldsymbol{K})\boldsymbol{r}} & \boldsymbol{r} \in I \\ \sum_{\ell,m} A_{\ell m}^{\boldsymbol{k}+\boldsymbol{K}} u_\ell(r, E_{1,\ell}) Y_m^\ell(\hat{\boldsymbol{r}}) & \boldsymbol{r} \in S_\alpha\,. \end{cases} \tag{3.27}$$

To improve the expansion a second type of functions is used. These functions are called *local orbitals* but they are not the same local orbitals (LOs) as mentioned above. Therefore they are referred to as los. The local orbitals (los) have the same

energy parameter $E_{1,\ell}$ as the corresponding APW's:

$$\phi_{lo}^{\ell m}(\boldsymbol{r}) = \begin{cases} 0 & \boldsymbol{r} \notin S_\alpha \\ \left(A_{\ell m}^{lo} u_\ell(r, E_{1,\ell}) + B_{\ell m}^{lo} \dot{u}_\ell(r, E_{1,\ell})\right) Y_m^\ell(\hat{\boldsymbol{r}}) & \boldsymbol{r} \in S_\alpha \,. \end{cases} \tag{3.28}$$

The coefficients $A_{\ell m}^{lo}$ and $B_{\ell m}^{lo}$ are determined by normalization of the functions and the condition that they have zero value at the sphere boundary. Considering these limitations the APW+lo functions are continuous at the sphere boundaries but they have kinks (i.e. the first derivatives are discontinuous). The LAPW functions, on the contrary, are continuous and smooth at the boundaries. The improvement of the APW+lo in contrast to the LAPW functions is that a lower value of $R_{MT} \cdot K_{max}$ is sufficient for convergence. As with LAPW semi-core states can once again be treated by local orbitals (LOs) as mentioned above. They are defined by

$$\phi_{LO}^{\ell m}(\boldsymbol{r}) = \begin{cases} 0 & \boldsymbol{r} \notin S_\alpha \\ \left(A_{\ell m}^{LO} u_\ell(r, E_{1,\ell}) + C_{\ell m}^{LO} u_\ell(r, E_{2,\ell})\right) Y_m^\ell(\hat{\boldsymbol{r}}) & \boldsymbol{r} \in S_\alpha \,. \end{cases} \tag{3.29}$$

APW+lo should be used for states that are difficult to converge, while LAPW should be used for all other states. For more details on the different methods see [16] and [17].

Not only the wave functions are expanded to a new basis, also the density and the potentials are expanded. In order to improve calculations all these expansions are further expanded to make use of the crystal symmetry. Therefore, inside the spheres point group symmetry is used and in the interstitial region the space group symmetry is used. Plane waves are expanded to symmetrized plane waves, called stars. This expansion is limited by a maximal reciprocal lattice vector G_{max}, which is chosen during the initialization process. In the spheres an expansion to lattice harmonics, which are symmetrized spherical harmonics, is used.

The Coulomb potential V_C (consisting of the Hartree potential V_H and the nuclear potential) is determined using the Poisson equation. In WIEN2k it is solved in reciprocal space by the program *lapw0*. In order to do so, the density is further expanded into multipoles q_{lm}.

3.2. Exchange-Correlation Functionals

In order to get a well converged calculation with reasonable results, using a good approximation for V_{xc} is crucial. There are many different methods how to calculate the exchange-correlation energy. To choose which one of them is the right one depends strongly on the system that is calculated. Usually the standard LDA approximation or the generalized gradient approximation (GGA) are good choices. But for strongly correlated electron systems or transition metals these approximations give wrong results. When investigating such materials more sophisticated methods have to be used, which increases the calculation time. In WIEN2k this can be done using on site LDA+U calculations, which includes Hubbard interaction, or by means of hybrid functionals. Recently, a modified Becke-Johnson potential was developed [3], which further improves results, especially of band gap calculations.

For the sake of consistency with literature, the electronic density is denoted as n in sections 3.2.1 and 3.2.2, while ρ is used in sections 3.2.3 and 3.2.4.

3.2.1. Generalized Gradient Approximation

There are different types of the generalized gradient approximation. The differences lie in the determination of certain parameters used in the approximation. Either they are determined semi-empirically such that certain experimental values are met, or they are determined by using mathematical conditions which are met by the exact functional. In the GGA reported by Perdew, Burke and Ernzerhof (PBE), see [18], the exchange-correlation functional is approximated as

$$E_{xc}^{GGA}[n_\uparrow, n_\downarrow] = \int d^3r n \epsilon_x^{unif}(n) F_{xc}(r_s, \zeta, s)\,. \tag{3.30}$$

Here, n is the electron density, $n_\uparrow$ and $n_\downarrow$ are the corresponding spin-densities. The exchange energy per particle of the uniform electron gas is $\epsilon_x^{unif} = -3e^2 k_F/4\pi$. r_s is the local Seitz radius for which $n = 3/4\pi r_s^3 = k_f^3/3\pi^2$ holds. $\zeta = (n_\uparrow - n_\downarrow)/n$ is the relative spin polarization. Finally, $s = |\nabla n|/2k_F n$ is a dimensionless density gradient. All the parameters in the PBE-GGA are fundamental constants and chosen to obey certain conditions mentioned in [18]. This method is the recommended one for using the generalized gradient approximation in WIEN2k.

3.2.2. LDA+U

For systems with highly correlated electrons, for example the 3d electrons in Ni, LDA and GGA give wrong results. Therefore, electron-electron interaction has to be treated in a different way. One possibility is to use the Hubbard model. It combines electron hopping between nearest neighbour lattice sites and Coulomb repulsion of electrons at the same site

$$H = \sum_{ij\sigma} t_{ij} c^{\dagger}_{i\sigma} c_{j\sigma} + U \sum_{i} n_{i\uparrow} n_{i\downarrow} \,. \tag{3.31}$$

The first sum is over nearest neighbours i and j, the parameter t_{ij} describes the electron hopping between two lattice sites. The $c^{\dagger}_{i\sigma}$ and $c_{i\sigma}$ are the creation and annihilation operators for an electron at site i with spin σ, respectively. U (also called Hubbard-U) describes the Coulomb interaction of two electrons with different spins at the same lattice site and $n_{i\sigma} = c^{\dagger}_{i\sigma} c_{i\sigma}$ is the occupation number operator. Because of the Hubbard-U this correction to LDA is called LDA+U.

In density functional theory the Hubbard model is used for correction of the LDA energy functional. This is usually done only for the orbital(s) containing the correlated electrons. Thus, the method is also called orbital potential method. In WIEN2k three different methods for LDA+U are implemented. The recommended one is described in detail in [19]. It is called LDA+U(SIC) because a self interaction correction (SIC) is included. The exchange correlation energy is modified such that in addition to the LDA energy an electron-electron interaction term according to the Hubbard model is added. Furthermore, as exchange is partially taken into account in LDA, a correction for double-counting is applied:

$$E_{LDA+U} = E_{LDA} + E_{Hub} - E_{dc} \,. \tag{3.32}$$

The total energy functional is derived in [19] and can be written as

$$\begin{aligned} E = E_{LDA} &- [UN(N-1)/2 - JN(N-2)/4] \\ &+ \frac{1}{2} \sum_{m,m',\sigma} U_{mm'} n_{m\sigma} n_{m'-\sigma} + \frac{1}{2} \sum_{m,m' \neq m,\sigma} (U_{mm'} - J_{mm'}) n_{m\sigma} n_{m'\sigma} \,. \end{aligned} \tag{3.33}$$

The index m is defined by $m = -\ell, \ldots, \ell$. The matrices $U_{mm'}$ and $J_{mm'}$ are defined

as follows:

$$U_{mm'} = \sum_k a_k F^k, \tag{3.34}$$

$$J_{mm'} = \sum_k b_k F^k, \tag{3.35}$$

$$a_k = \frac{4\pi}{2k+1} \sum_{q=-k}^{k} \langle lm \,|\, Y_{kq} \,|\, lm \rangle \left\langle lm' \,\middle|\, Y^*_{kq} \,\middle|\, lm' \right\rangle, \tag{3.36}$$

$$b_k = \frac{4\pi}{2k+1} \sum_{q=-k}^{k} |\, \langle lm \,|\, Y_{kq} \,|\, lm' \rangle \,|^2 . \tag{3.37}$$

The F^k are Slater integrals, see (3.43). For the calculation of d electrons only F^0, F^2 and F^4 are needed, see [19]. For LDA+U they are expressed in terms of the parameter U. This expression and how they are related to each other is described in [19]. One also has to keep in mind that for different materials the value of U is also different. The $n_{m\sigma} n_{m'-\sigma}$ are also denoted as $n^{\sigma,-\sigma}_{m,m'}$ and are the density matrices.

To perform this orbital calculation in WIEN2k the density matrices are needed. Therefore, two additional steps in the SCF cycle are included. One for doing the orbital calculation and one for calculating the density matrix. For more details on how these calculations using the density matrix are done see [20].

For computational reasons in WIEN2k it is recommended to use an *effective* parameter $U_{eff} = U - J$ and set the parameter $J = 0$, see [1].[2]

3.2.3. Hybrid functionals

In recent years the approximation of the exchange-correlation functional was further improved. A short overview of different hybrid functionals and the comparison of calculation results for several materials is given in [2]. In this work two different hybrid functionals, called PBE0 and B3PW91, were used.

The first one, PBE0, is described in [22, 23]. There, also a short overview of the shortcomings of the standard PBE-GGA functional is given. The PBE0 exchange-

[2]Note that, due to implementation details, one does not use $U - J/2$ as would be suggested by equation (3.33), see [21].

correlation functional is

$$E_{xc}^{PBE0}[\rho] = E_{xc}^{PBE}[\rho] + \frac{1}{4}\left(E_x^{HF}[\psi_{sel}] - E_x^{PBE}[\rho_{sel}]\right) . \tag{3.38}$$

ψ_{sel} and ρ_{sel} are the wave function and electron density of the selected electrons, in this work the Ni 3d electrons. The PBE0 functional consists of the PBE-GGA exchange-correlation functional (3.30) for the total density and for the selected electrons a Hartree-Fock exchange functional replaces the PBE-GGA exchange functional. The factor $\frac{1}{4}$ can be determined from fourth order perturbation theory, see [2] and references therein. In LDA+U the correction for double-counting was only approximate, as occupation numbers for atomic like orbitals are used. When using hybrid functionals the correction for double-counting is exact as the correction is only done for the electron density of the selected electrons.

The second hybrid functional used in this work is the B3PW91-functional:

$$\begin{aligned} E_{xc}^{B3PW91}[\rho] = E_{xc}^{LDA}[\rho] &+ 0.2\left(E_x^{HF}[\psi_{sel}] - E_x^{LDA}[\rho_{sel}]\right) \\ &+ 0.72\left(E_x^{B88}[\rho] - E_x^{LDA}[\rho]\right) \\ &+ 0.81\left(E_c^{PW91}[\rho] - E_c^{LDA}[\rho]\right) . \end{aligned} \tag{3.39}$$

The functional is described in detail in [24]. E_x^{LDA} is the exchange part, while E_c^{LDA} is the correlation part of the LDA energy functional (3.11). E_x^{B88} is a GGA exchange energy functional proposed by Becke, see [25]. E_c^{PW91} is the correlation part of the GGA functional proposed by Perdew and co-workers, see [26, 27]. The second term of the B3PW91 hybrid functional is again a replacement by a Hartree-Fock exchange for the selected electrons. The third term is a gradient correction to LDA for exchange and the fourth term is a gradient correction for correlations. The three factors (0.2, 0.72 and 0.81) are chosen to match experimental thermochemical data, see [2].

The Hartree-Fock energy E_x^{HF} is calculated as

$$E_x^{HF}[\psi_{sel}] = -\frac{1}{2}\sum_{\sigma}\sum_{m_1,m_2,m_3,m_4} n_{m_1,m_2}^{\sigma} n_{m_3,m_4}^{\sigma} \langle m_1 m_3 \,|\, V_{ee} \,|\, m_4 m_2 \rangle \tag{3.40}$$

with n_{m_i,m_j}^{σ} the density matrix, $m_i = -\ell, \ldots, \ell$ and σ the spin index. This calculation is done only for the selected electrons with the angular momentum ℓ. $V_{ee} = 1/|\boldsymbol{r}_1 - \boldsymbol{r}_2|$

is the unscreened Coulomb potential. The integrals are calculated in WIEN2k as

$$\langle m_1 m_3 \,|\, V_{ee} \,|\, m_4 m_2 \rangle = \sum_{k=0}^{2\ell} a_k(m_1, m_2, m_3, m_4) F^k \,, \tag{3.41}$$

with

$$\begin{aligned} a_k(m_1, m_2, m_3, m_4) = \frac{4\pi}{2k+1} \sum_{q=-k}^{k} & \langle Y_{lm_1} \,|\, Y_{qk} \,|\, Y_{lm_4} \rangle \\ & \times \left\langle Y_{lm_3} \,\middle|\, Y^*_{qk} \,\middle|\, Y_{lm_2} \right\rangle \end{aligned} \tag{3.42}$$

and F^k the Slater integrals

$$F^k = \int_0^{R_{MT}} \int_0^{R_{MT}} \chi^2_\ell(\boldsymbol{r_1}) \chi^2_\ell(\boldsymbol{r_2}) \frac{r^k_<}{r^k_>} r_1^2 r_2^2 dr_1 dr_2 \,. \tag{3.43}$$

In equation (3.43) the $r_< = \min(r_1, r_2)$, $r_> = \max(r_1, r_2)$ and the $\chi_\ell(\boldsymbol{r})$ are radial functions whose calculation is illustrated in [16, 28]. In contrast to LDA+U the Slater integrals are calculated explicitly and are not adjustable parameters. Furthermore, when using hybrid functionals, the double count correction is done in an exact way. Thus, calculation results are improved for many materials compared to LDA+U, but at the cost of calculation time.

3.2.4. Modified Becke-Johnson Potential

In 2009 a modified Becke-Johnson (mBJ) exchange potential, based on an exchange potential described in [29], was developed by Tran and co-workers [3]. This potential is used together with the LDA correlation functional (mBJLDA). The potential is defined as:

$$V^{MBJ}_{x,\sigma}(\boldsymbol{r}) = c V^{BR}_{x,\sigma}(\boldsymbol{r}) + (3c-2) \frac{1}{\pi} \sqrt{\frac{5}{12}} \sqrt{\frac{t_\sigma(\boldsymbol{r})}{\rho_\sigma(\boldsymbol{r})}} \,, \tag{3.44}$$

where $\rho_\sigma(\boldsymbol{r})$ is the electron spin density and

$$t_\sigma(\boldsymbol{r}) = \frac{1}{2} \sum_{i=1}^{N_\sigma} \nabla \psi^*_{i,\sigma}(\boldsymbol{r}) \cdot \nabla \psi_{i,\sigma}(\boldsymbol{r}) \tag{3.45}$$

is the kinetic energy density. $V_{x,\sigma}^{BR}(\boldsymbol{r})$ is a potential proposed by Becke and Roussel, for the definition see [3, 30]. It depends on a nonlinear equation involving ρ_σ, $\nabla\rho_\sigma$, $\nabla^2\rho_\sigma$ and t_σ. The factor c depends on the square root of $|\nabla\rho|/\rho$:

$$c = \alpha + \beta \left(\frac{1}{V} \int \frac{|\nabla\rho(\boldsymbol{r}')|}{\rho(\boldsymbol{r}')} d^3\boldsymbol{r}' \right)^{1/2} , \tag{3.46}$$

where V again is the volume of the unit cell and the integration is carried out over this volume. In the SCF cycle of WIEN2k the program *lapw0* is executed a second time to do this integration. The parameters α and β are chosen such that the band gap of different solids is resembled in the best way, i.e. the mean absolute relative error is minimized [3].

In contrast to LDA+U and hybrid functionals, the modified Becke-Johnson potential is used for all electrons of the system. The potential $V_{x,\sigma}^{MBJ}$ is included in the exchange-correlation part of the Kohn-Sham Hamiltonian $\hat{H}_{KS} = \hat{T} + \hat{V}_H + \hat{V}_{xc} + \hat{V}_{ext}$ (usually in LDA, see (3.11)). According to [31], in WIEN2k the kinetic energy density is calculated as

$$t_\sigma(\boldsymbol{r}) = \sum_{i=1}^{N_\sigma} \epsilon_{i,\sigma} |\psi_{i,\sigma}(\boldsymbol{r})|^2 - V_{eff,\sigma}^{KS}(\boldsymbol{r})\rho_\sigma(\boldsymbol{r}) + \frac{1}{4}\nabla^2\rho_\sigma(\boldsymbol{r}) \tag{3.47}$$

where $V_{eff,\sigma}^{KS}(\boldsymbol{r}) = V_H + V_{xc} + V_{ext}$ is the effective potential of the Kohn-Sham equations. This expression of $t_\sigma(\boldsymbol{r})$ is equivalent to equation (3.45) [31]. To evaluate (3.47) $V_{eff,\sigma}^{KS}(\boldsymbol{r})$ of the previous iteration of the SCF cycle is used. To generate a starting value for $V_{eff,\sigma}^{KS}(\boldsymbol{r})$ a single SCF iteration has to be carried out before starting of a full SCF cycle using the mBJLDA. Because of this mutual dependence of $V_{eff,\sigma}^{KS}(\boldsymbol{r})$ and $t_\sigma(\boldsymbol{r})$, calculations using the modified Becke-Johnson potential are more difficult to converge than GGA calculations. Therefore, in some cases a different mixing scheme has to be used to mix ρ_{in} and ρ_{out}.

The definition in (3.44) is just a potential and there is no exchange functional $E_x[\rho]$ for that $V_{x,\sigma}^{MBJ} = \delta E_x[\rho]/\delta\rho_\sigma$ holds. Thus, to calculate structural properties a full SCF cycle using a GGA functional should be carried out before the mBJLDA is used in another SCF cycle for band structure calculations.

Calculations using the mBJLDA are much more time-consuming than standard GGA calculations because the SCF cycle has to be carried out twice. But the resulting density of states shows a much better agreement with experiments.

3.3. Program Flow

3.3.1. Initialization process

To start a calculation using WIEN2k a *case.struct*–file has to be created. In this file the crystal properties, like structure type, lattice constants, atomic positions and the radii of the muffin-tin spheres R_{MT} are given.

The program *nn* calculates distances to neighbouring atoms and checks for overlapping atomic spheres. It also verifies that equivalent atom positions are entered correctly in the *case.struct*–file.

The spacegroup of the structure and the pointgroup of the non-equivalent sites are calculated by *sgroup*.

symmetry generates all symmetry operations for the given structure. It also determines the pointgroup of each atomic site and generates the respective symmetry operations. Furthermore, the expansion for the lattice harmonics is calculated.

The program *lstart* generates free atomic densities and potentials. It prints out a warning if density of the core states leaks out of the muffin-tin spheres. Also, whether different orbitals are treated as core-, semi-core-, or valence-states is determined. The program asks which method should be used for calculation of the exchange-correlation potential and at which energy core-states are separated from valence-states. In the input file *case.inst* the electron configuration of each atom, as well as the information which electrons should be treated as spin-up or spin-down electrons, is given.

kgen generates a k-mesh in the irreducible wedge of the Brillouin zone, which is used in a modified tetrahedron scheme for further calculations, see [32]. It takes the number of k-points as input parameter.

dstart generates the crystalline starting density for the SCF cycle by superposition of the atomic densities calculated in *lstart*.

3.3.2. Self Consistent Field Cycle

Each SCF iteration is started with *lapw0* which uses an input density ρ (either from *dstart* or from the output of a previous iteration) to create the total potential V_{tot} as a sum of the Coulomb potential V_C and the exchange-correlation potential V_{xc}. The program also calculates the expansion of the Coulomb potential into multipole moments, while the exchange-correlation potential is calculated numerically using lattice harmonics inside the muffin-tin spheres and using a fast Fourier transformation outside.

The eigenvectors and eigenvalues of the valence bands are calculated by *lapw1* by means of diagonalisation. Different calculation schemes are implemented. In this program the LAPW or APW+lo expansion is performed.

The program *lapw2* calculates the Fermi energy and generates the expansion of the valence densities with respect to the crystal symmetry. The charges or partial charges (decomposed with respect to quantum number ℓ) inside the muffin-tin spheres are calculated by integration over the Brillouin zone.

lcore computes the eigenvalues for core states and the corresponding densities.

The program *mixer* calculates the overall density by summing up the core-, semi-core- and valence densities. It then mixes this total density with the input density to generate a new output density. This is done in order to stabilize the SCF cycle. Several mixing schemes are implemented. The simplest one is a straight mixing according to $\rho_{new} = (1 - Q)\rho_{old} + Q\rho_{total}$, with Q as a mixing factor. Also several multi-secant mixing schemes are implemented. For details see [1] and references therein.

All the calculations of the SCF iteration are repeated until chosen convergence criteria, like convergence of the total energy or charge convergence, are met. When performing spin-polarized calculations *dstart*, *lapw1*, *lapw2* and *lcore* are called separately for each spin direction.

For calculations using orbital potentials like LDA+U or when hybrid functionals are used, two other programs are invoked during each SCF iteration. The program *orb* calculates the orbital potential, which is non-zero inside the muffin-tin spheres only and depends on the quantum numbers ℓ and m. *lapwdm* computes the density matrices, which are needed for this type of calculations.

3.4. Calculating Crystal-properties

After finishing the SCF cycle, different crystal properties can be calculated. In this work calculations of the density of states (DOS) and electron energy loss spectra were performed.

3.4.1. Density of States

The density of states $D(E)$ gives the number of electronic states per unit energy range. As an example the DOS of a free three-dimensional electron gas is calculated, following the derivation in [33]. The Schrödinger equation of a free particle is

$$-\frac{\hbar^2}{2m}\left(\frac{\partial^2}{\partial x^2}+\frac{\partial^2}{\partial y^2}+\frac{\partial^2}{\partial z^2}\right)\psi_{\boldsymbol{k}}(\boldsymbol{r})=\epsilon_{\boldsymbol{k}}\psi_{\boldsymbol{k}}(\boldsymbol{r})\,, \tag{3.48}$$

whose solution are the wave functions

$$\psi_{\boldsymbol{k}}(\boldsymbol{r})=\frac{1}{\sqrt{V}}e^{i\boldsymbol{k}\boldsymbol{r}}\,. \tag{3.49}$$

Assuming periodic boundary conditions

$$\psi_{\boldsymbol{k}}(x+L,y,z)=\psi_{\boldsymbol{k}}(x,y,z) \tag{3.50}$$

and similar for the other two dimensions, the components of the wavevector $\boldsymbol{k}$ satisfy

$$k_i=\frac{2n\pi}{L} \tag{3.51}$$

with n as any integer. The energy is then:

$$\epsilon_{\boldsymbol{k}}=\frac{\hbar^2k^2}{2m_e}=\frac{\hbar^2}{2m_e}(k_x^2+k_y^2+k_z^2)\,. \tag{3.52}$$

In the ground-state of a N-particle free electron system the occupied states represent a sphere in $\boldsymbol{k}$-space. The vector $\boldsymbol{k}_F$ corresponds to the highest occupied states with the energy

$$\epsilon_F=\frac{\hbar^2}{2m_e}k_F^2 \tag{3.53}$$

and points to the surface of the sphere. Only one wavevector $\boldsymbol{k}$ is allowed in the volume element $(2\pi/L)^3$ in the $\boldsymbol{k}$-space. Therefore, in the sphere S with volume $4\pi k^3/3$ the number of allowed states is

$$N_S = 2 \cdot \frac{4\pi k^3/3}{(2\pi/L)^3} = \frac{V_S}{3\pi^2} k^3 \,, \tag{3.54}$$

where the factor 2 arises from the two possible spin directions. With this

$$k = (3\pi^2 N_S/V_S)^{1/3} \tag{3.55}$$

and

$$\epsilon_{\boldsymbol{k}} = \frac{\hbar^2}{2m_e}(3\pi^2 N_S/V_S)^{2/3} \tag{3.56}$$

hold. Now equation (3.56) is used to calculate the DOS:

$$D(\epsilon_{\boldsymbol{k}}) = \frac{\mathrm{d}N_S}{\mathrm{d}\epsilon_{\boldsymbol{k}}} = \frac{V_S}{2\pi^2} \cdot \left(\frac{2m_e}{\hbar^2}\right)^{3/2} \cdot \epsilon_{\boldsymbol{k}}^{1/2} \,. \tag{3.57}$$

In the simulation package WIEN2k the DOS is determined by counting the electrons. This is done by integrating the charge density over the Brillouin zone using the program *tetra*. The integration is performed using the modified tetrahedron method described in [32]. Not only the total DOS is calculated but also the partial DOS, which is the atomic DOS for every atom in the unit cell. This atomic DOS is further decomposed with respect to the quantum numbers ℓ and m. In order to do so, the charge density has to be decomposed in the same way. This is done by the program *lapw2* when invoked using the switch *-qtl*. The density

$$q_{tot} = q_i + \sum_t \sum_\ell q_{t\ell} \,, \tag{3.58}$$

where q_i is the interstitial charge density and the first sum covers all atoms t in the unit cell. Depending on certain parameters, defined during compilation of WIEN2k, the q_{tl} are further expanded with respect to the quantum number m.

3.4.2. Energy Loss Near Edge Structure

Calculation of the energy loss near edge structure (ELNES) is done by the program *TELNES.2* which is described in [34]. The probability of a beam electron to be scattered into a direction described by a solid angle Ω, transferring the energy E and momentum q, is called double differential scattering cross-section (DDSC). Using Fermi's golden rule and the assumption that the interaction of the beam electrons with the nuclei does not contribute to the inelastic scattering, it can be written as [34]

$$\frac{\partial^2\sigma}{\partial E\partial\Omega}(E,\boldsymbol{q}) = \frac{4\gamma^2}{a_0^2}\frac{k_F}{k_I}\frac{1}{q^4}\sum_{I,F}\left|\left\langle I\left|\sum_{j=1}^{N} e^{i\boldsymbol{q}(\boldsymbol{r}-\boldsymbol{r}_j)}\right|F\right\rangle\right|^2 \delta(E_I - E_F - E)\,. \tag{3.59}$$

I denotes initial states and F denotes final states. The N sample electrons occupy the positions $\boldsymbol{r}_j$ while the beam electrons are described by $\boldsymbol{r}$. It is noted that in this formula $\boldsymbol{q}$ describes the momentum transfer and must not be confused with the densities in equation (3.58). For more details see section 5.3 and [34, 35]. This formula can be further simplified such that it depends on the unoccupied density of states $\chi_{l_F}(E)$ and a matrix element $M_{l_F}(\boldsymbol{q},E)$

$$\frac{\partial^2\sigma}{\partial E\partial\Omega}(E,\boldsymbol{q}) = \sum_{l_F}\left|M_{l_F}(\boldsymbol{q},E)\right|^2\chi_{l_F}(E)\,, \tag{3.60}$$

where the sum is over all final states with orbital quantum number l_F. This is described in [34].

Some further approximations are made in order to simplify calculations: as initial states are strongly localized, the description of the final states is only needed inside the muffin-tin spheres. The incoming electron wave is assumed to be a plane wave. And finally, diffraction effects and channelling conditions are also not taken into account.

As input parameters of the program *TELNES.2* one has to specify the atom, as well as n and l values of the initial state of the edge for which the spectrum should be calculated. Furthermore, the energy of the edge, the incident beam energy, an energy window in which the spectrum is calculated, the energy step size and the spectrometer broadening have to be specified. Also, the convergence and collection

semi-angles need to be provided as input parameters.

After calculating the energy loss spectra they have to be broadened using the program *broadening*. It convolves the calculated spectrum with a broadening function. This function is a Lorentzian for broadening due to the finite lifetimes of initial and final states. Its width for initial states is taken from atomic data tables [36]. The width for the final states is energy dependent and can be calculated in four different ways. They can be assumed to have constant width, to depend linearly with the energy above the edge threshold, to show a quadratic energy dependence, or to show a sophisticated behaviour described in [37]. In addition, spectrometer broadening is taken into account by convolution with a Gaussian function. All these models are described in [34, 37–39].

4. Simulations and Interpretation

The simulations were performed using the full potential augmented plane wave code WIEN2k in its version 10.1 [1]. The simulation package was implemented on a PC equipped with an AMD Athlon 64 3200+ with 2 GHz and 2 GB RAM.

The input for structure type, lattice parameters and atomic positions to calculate NiO is shown in Table 4.1. For details on the program flow of the simulations see section 3.3 and [1, 16], as well as references therein.

According to [39], simulations should be started using a small number of k-Points This number should then be increased until no further changes in the ELNES-spectra were observed. In this work simulations were started using 100 k-points. This number was increased until 2000 k-points were reached. All further calculations were then performed using 2000 k-points and a plane wave cut-off-parameter RKMAX of 7. The atomic sphere radii of both Ni-atoms were 2.09 a.u. and 1.85 a.u. for the O-atom which corresponds to 0.11 nm and 0.10 nm, respectively. All calculations were performed using spin polarization. Simulations were done systematically with standard GGA, LDA+U, two different hybrid potential methods (PBE0 and B3PW91) and a modified Becke-Johnson potential. Each method is described in detail in chapter 3.2. After convergence of the SCF cycle the DOS and ELNES-spectra were calculated in order to compare them with experimental values.

Lattice type	Lattice parameters	Atom positions
R	a = b = 2.966163 Å	Ni1: $x = 0,\ y = 0,\ z = 0$
	c = 14.531171 Å	Ni2: $x = 0.5,\ y = 0.5,\ z = 0.5$
	$\alpha = \beta = \gamma = 90°$	O: $x = \pm 0.25,\ y = \pm 0.25,\ z = \pm 0.25$

Table 4.1.: Input data for calculation of NiO using WIEN2k. Atom positions are given in local coordinates of the unit cell.

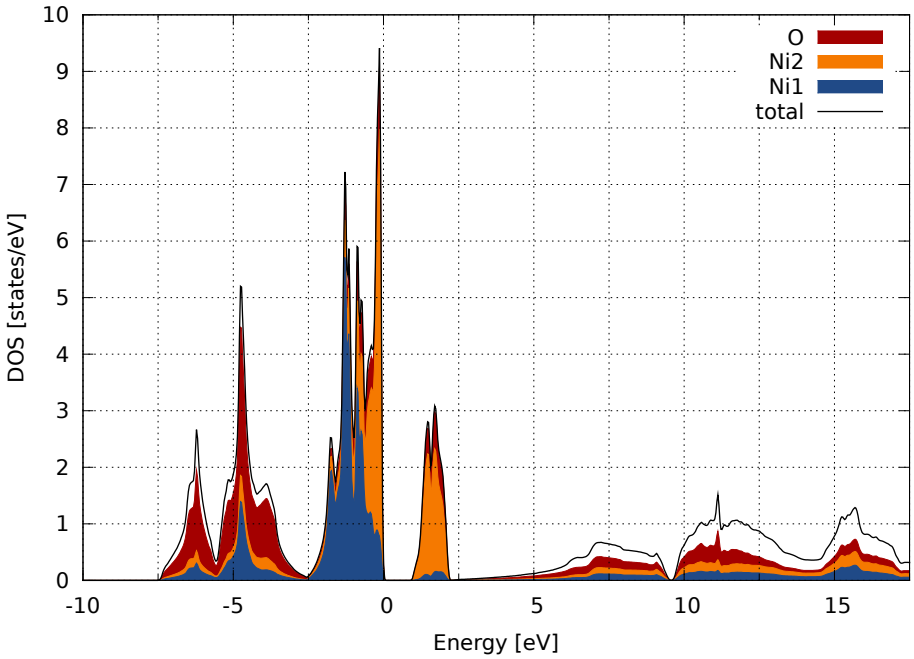

Figure 4.1.: Total DOS calculated using the GGA method. The energy is plotted with respect to the Fermi energy E_F. The total atomic-DOS are marked in different colours. The interstitial DOS is marked as white area. The different partial DOS are plotted cumulative, therefore they correspond to the area plotted in the respective colour. This plotting scheme is used in all the following DOS-plots.

4.1. Density of States

After the SCF cycle finished, using the convergence criterion that the total energy does not change more than 0.0001 Ry, the DOS was calculated using the program *tetra*. The calculated total DOS was then plotted and the total atomic-DOS inside the muffin-tin spheres were marked using different colours. The interstitial DOS outside the muffin-tin spheres was marked as the white area beneath the graph. The plots of the DOS can be used to read out the fundamental band gap and compare it to experimental values.

The total DOS calculated using the standard GGA method is shown in figure 4.1. It can be seen that the GGA method gives a bandgap of about 1 eV. Thus, it severely underestimates the experimental bandgap of $4.0 - 4.3$ eV (see [2] and references therein, as well as [40]).

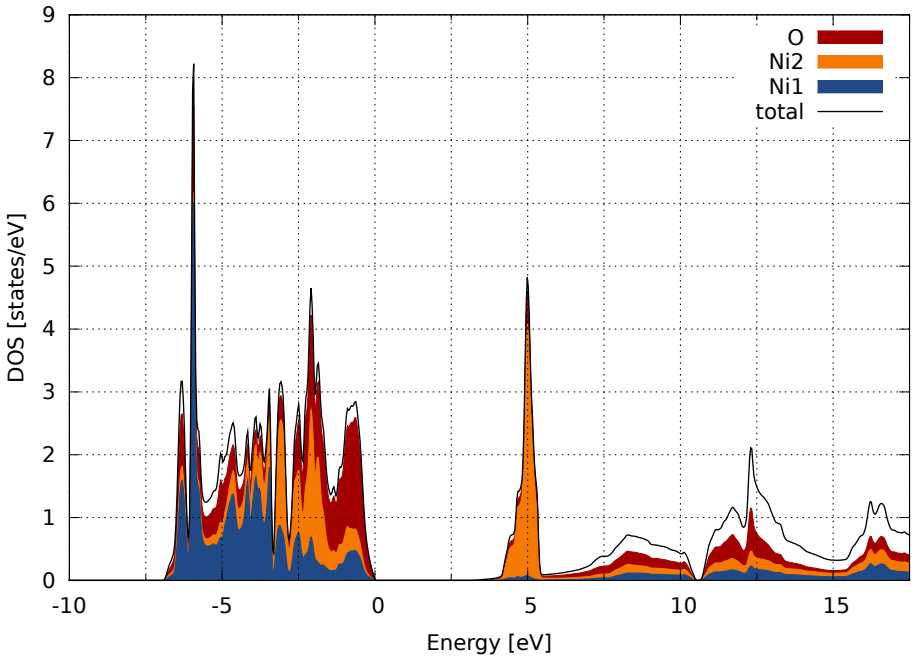

Figure 4.2.: Total DOS calculated using the LDA+U method.

In figure 4.2 the total DOS calculated using the LDA+U method is shown. Like in [2] the value for U_{eff} was 7.05 eV = 0.52 Ry. With a calculated band gap width of 3.2 eV significant improvement is evident. Also the general shape of the valence band states is different to the GGA-calculation.

The total DOS calculated with two different hybrid potential methods, namely B3PW91 and PBE0 functionals is shown in figures 4.3 and 4.4. It can be seen that in both cases the band gap width of 2.8 eV still underestimates the experimental values of 4.0 eV to 4.3 eV. Both plots are very similar with only slight differences in the valence band and the unoccupied Ni 3d states between Fermi level an $E_F + 5$ eV.

Figure 4.5 shows the calculated total DOS using the modified Becke-Johnson potential. It can be seen that this simulation method results in a band gap of 4.16 eV.

Thus, from all the potentials applied in this work, the modified Becke-Johnson potential is the only one which gives a band gap width similar to the experimentally acquired one. The DOS of the valence band is very similar to the LDA calculation and also similar to the hybrid potential simulations, but with the mBJLDA calculation the unoccupied Ni 3d states are shifted to higher energies. Compared to the LDA+U simulation the structure of the valence band is clearly different which is mainly due

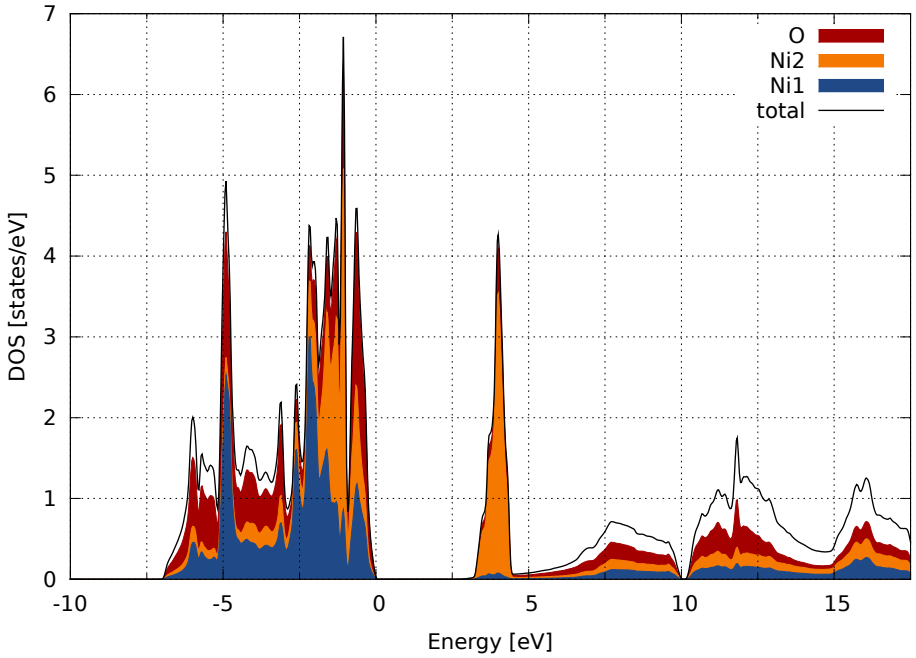

Figure 4.3.: Total DOS calculated using the hybrid potential B3PW91.

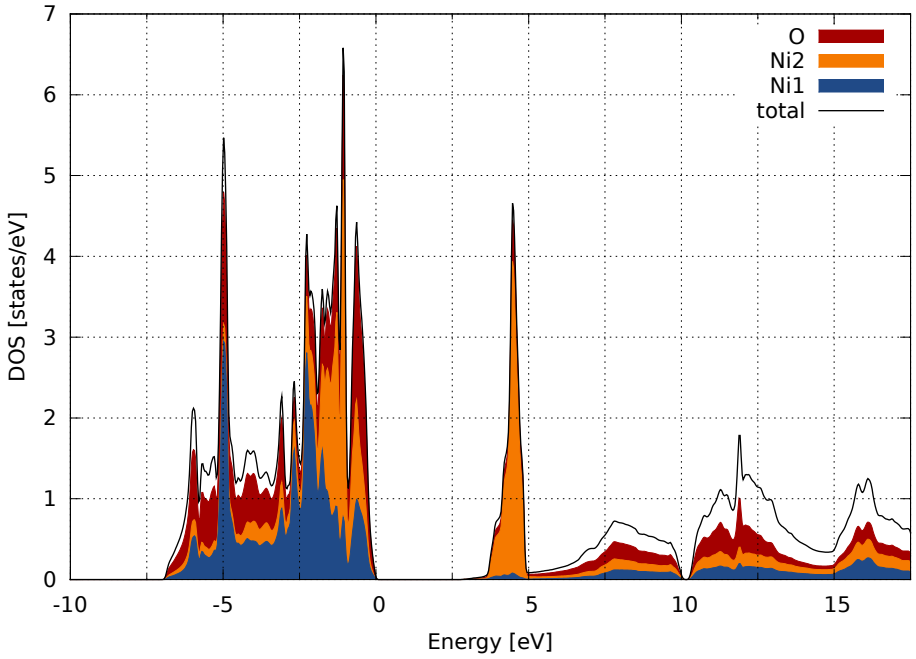

Figure 4.4.: Total DOS calculated using the hybrid potential PBE0.

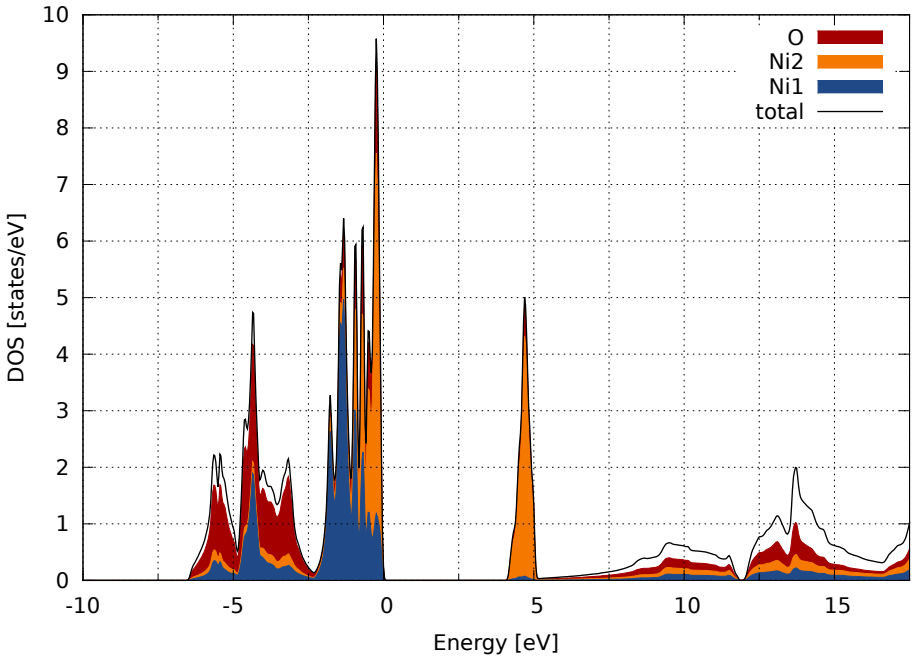

Figure 4.5.: Total DOS calculated using the modified Becke-Johnson potential.

to differences in the Ni 3d DOS. Figures 4.6 and 4.7 show the O and Ni atomic-DOS calculated using the modified Becke-Johnson potential. The l-projected DOS (s, p, d) is marked in different colours. When calculating the total atomic-DOS using *tetra* the multiplicity of the atoms in the unit cell is considered. For the l-projected DOS it is not, however. Therefore, the total DOS resembles the sum over the total atomic-DOS of each atom and the interstitial DOS. On the other hand, the total atomic-DOS is the sum of the l-projected DOS times the multiplicity. From figures 4.6 and 4.7, where the Oxygen 2p and the Nickel 3d states occupy the same energies, a p-d hybridization of the valence band, mainly of O 2p and majority spin Ni 3d, is evident. These are the states between $E_F - 6.0$ eV and the Fermi level. The conduction band, which is the energy region between 4 and 15 eV above Fermi level, also shows a small amount of p-d hybridization. Furthermore, the split of the minority spin Ni 3d states into two Hubbard-subbands at and above Fermi level is shown in figure 4.7. Thus, the mBJLDA-calculation is in agreement with [13] where NiO is described as a insulator with mixed Mott-Hubbard and charge-transfer characteristics.

As the main focus of this Thesis lies on electron energy loss spectroscopy, attention has to be directed to the structures above Fermi-level. In all calculation methods the

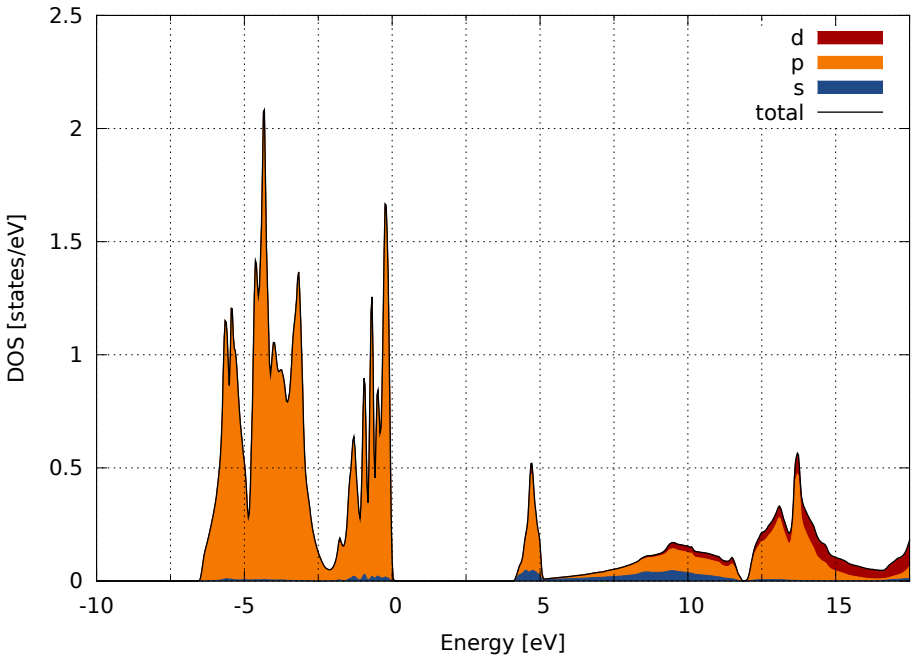

Figure 4.6.: Oxygen atomic-DOS calculated using the modified Becke-Johnson potential. The ℓ-projected DOS is plotted cumulative.

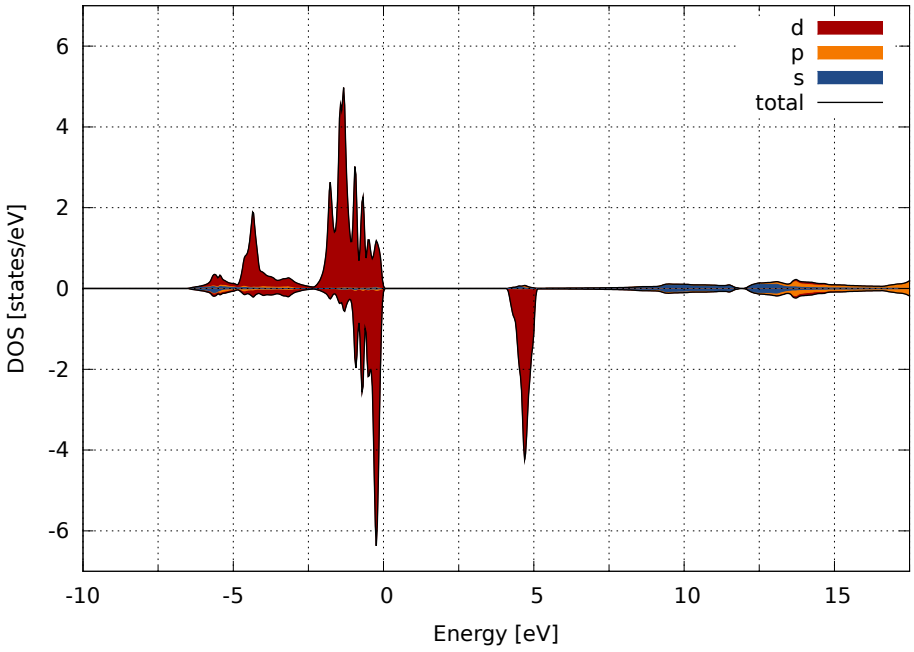

Figure 4.7.: Nickel atomic-DOS (ℓ-projected) calculated using the mBJLDA. Majority spins are plotted on positive ordinate, minority spins on negative ordinate.

shape of these structures are similar but peak positions and relative intensities are different. This gives rise to different near edge structures in the energy loss spectra, which will be discussed in section (ELNES).

4.2. Energy Loss Near Edge Structure

ELNES spectra were calculated using the program *TELNES.2*. All the following calculations were done using 200 keV beam energy, a collection semi-angle of 10.0 mrad and a convergence semi-angle of 0.01 mrad. A value of 1.4 eV was taken for the spectrometer broadening according to the full width at half maximum (FWHM) of the experimentally measured zero loss peak (ZLP). An energy window of 50 eV and a stepsize of 0.05 eV was used.

After calculating the spectra the program *broadening* is invoked. It applies a Lorentzian broadening for core and valence life times, as well as a Gaussian broadening for spectrometer broadening. The input file is generated automatically by *TELNES.2* and can be modified if needed.

In figure 4.8 a comparison of the Oxygen K-edge ELNES calculated with different exchange-correlation functionals is shown. As the Oxygen K-edge electron energy loss spectrometry (EELS) probes the excitation of 1s electrons, dipole allowed transitions are those into p-states. Therefore the shape of the ELNES should be similar to the p-projected DOS above the Fermi-level, except for effects like broadening (see below).[1] Furthermore, an experimentally acquired spectrum is plotted. It was acquired using a FEI TECNAI G^2 20 microscope with a LaB_6 cathode (referred to as G20), operated at 200 kV and equipped with a GATAN GIF 2001 energy filter. All the spectra are aligned at the first peak. It is evident that by using different functionals a change in peak positions and relative intensities can be seen. This results from differences in the Oxygen p-DOS above the Fermi energy which are shown in figure 4.9. It is also clear from figure 4.8 that though the shape of the spectra is reproduced well, the peak positions are not resembled very well. Furthermore, using LDA+U and hybrid exchange-correlation functionals the relative intensity of the first

[1] The hole left by the excited core electron can change the electronic structure of the crystal. Usually a core-hole calculation with supercells has to be performed to take these changes into account. According to [41] the effect of the core-hole is not always visible. In [42] it is reported that considering the core-hole does not change the resulting spectra. Therefore, due to the high computational costs in the following no core-hole calculations are conducted.

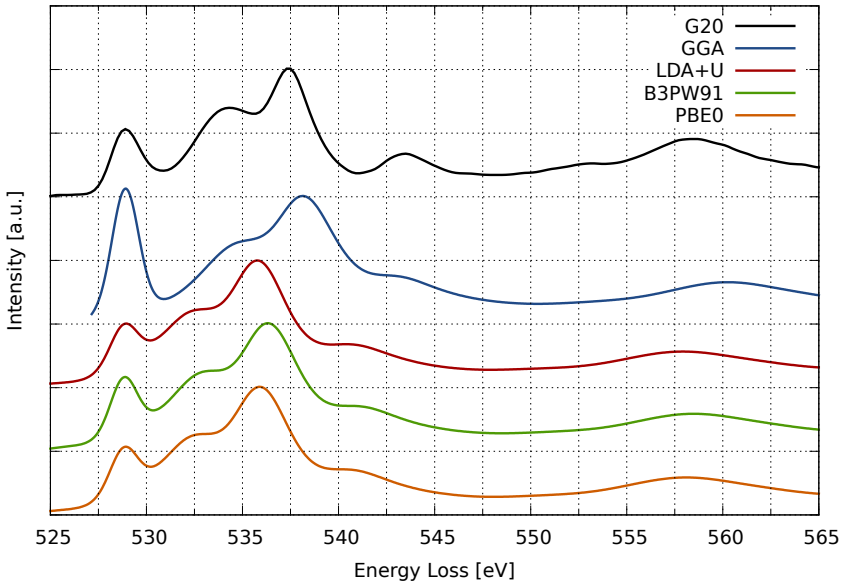

Figure 4.8.: Oxygen K-edge ELNES calculated using different exchange-correlation functionals compared to experimental spectrum. The spectra were shifted vertically for better visibility.

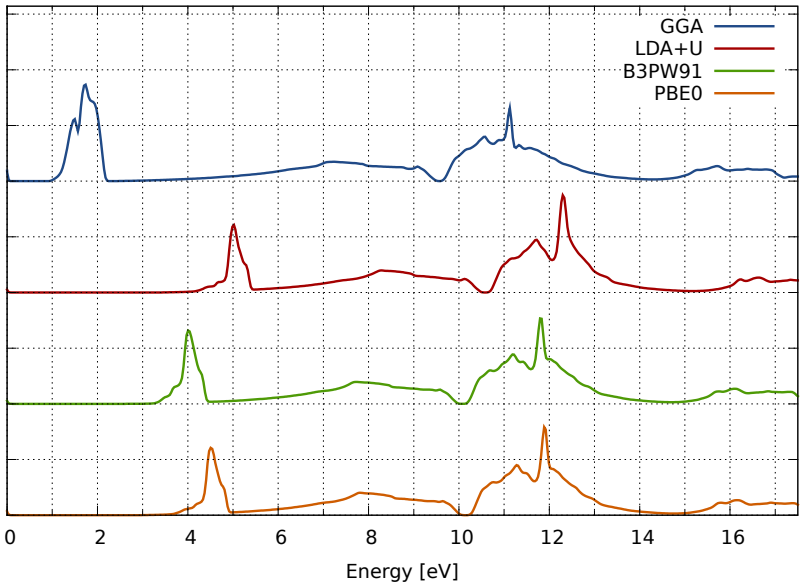

Figure 4.9.: Comparison of the O p-projected DOS above Fermi level calculated using different exchange-correlation functionals. The spectra were shifted vertically for better visibility.

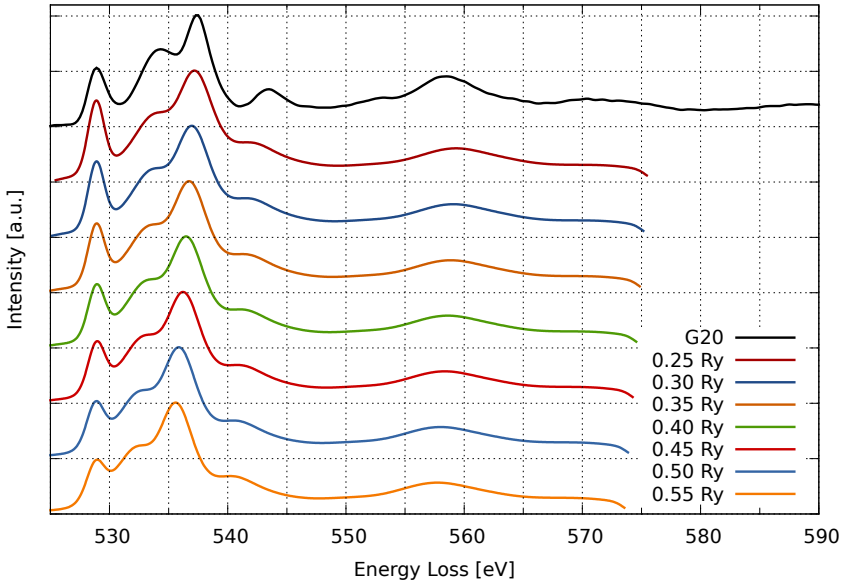

Figure 4.10.: Oxygen K-edge ELNES calculated using the LDA+U functional and different values of U_{eff}, ranging from 0.25 Ry to 0.55 Ry compared to experimental spectrum. The spectra were shifted vertically for better visibility.

peak is underestimated, whereas using the GGA functional the peak intensity is far overestimated.

In [43] different values of U_{eff} are listed, so in figure 4.10 Oxygen K-ELNES calculations for different values of U_{eff}, ranging from 0.25 eV to 0.55 eV, are compared. With increasing U_{eff} the relative intensity of the first peak as well as the distance to the main peak decreases. However, using different values of U_{eff} does not improve the agreement between calculated and experimental spectrum. In [42] the peak positions for a specific value of U_{eff} is changed by modifying the magnetic moments of the Nickel atoms in the calculation. This is done by changing a "temperaturelike" parameter of the SCF cycle. However, this is not a physically correct procedure because these changes correspond to a heating of the crystal to 15000 K.

Figure 4.11 shows a comparison of the experimentally measured Oxygen K-ELNES and the simulation calculated using the mBJ potential. It can be seen that the peak positions and the relative intensities are resembled very well. Altogether both spectra show a very good agreement. The differences can be attributed to shortcomings in the calculation of the broadening of the spectra, see for example [37, 38]. A comparison

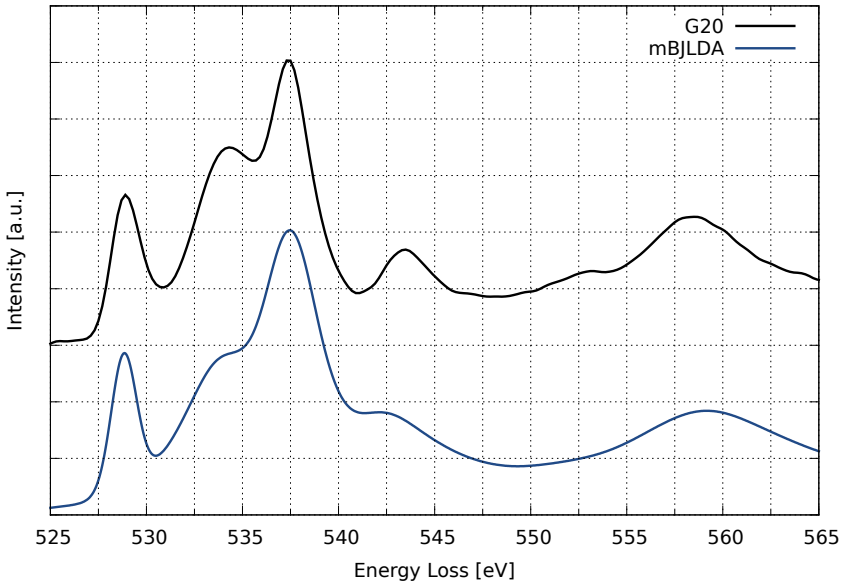

Figure 4.11.: Oxygen K-edge ELNES calculated using the modified Becke-Johnson potential compared to experimental spectrum. The spectra were shifted vertically for better visibility.

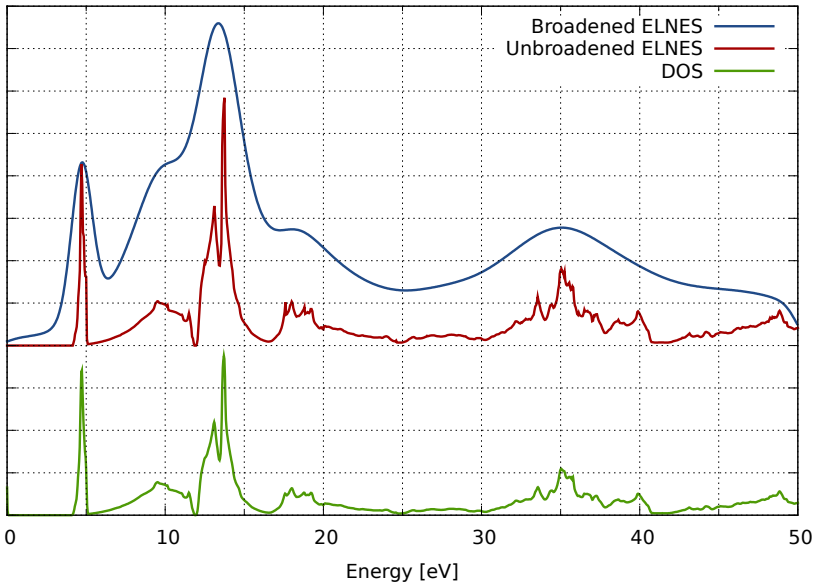

Figure 4.12.: Broadened and unbroadened O K-edge ELNES compared to O p-projected DOS. For the ELNES the energy beyond edge onset is plotted, while for the DOS it is the energy above Fermi-level.

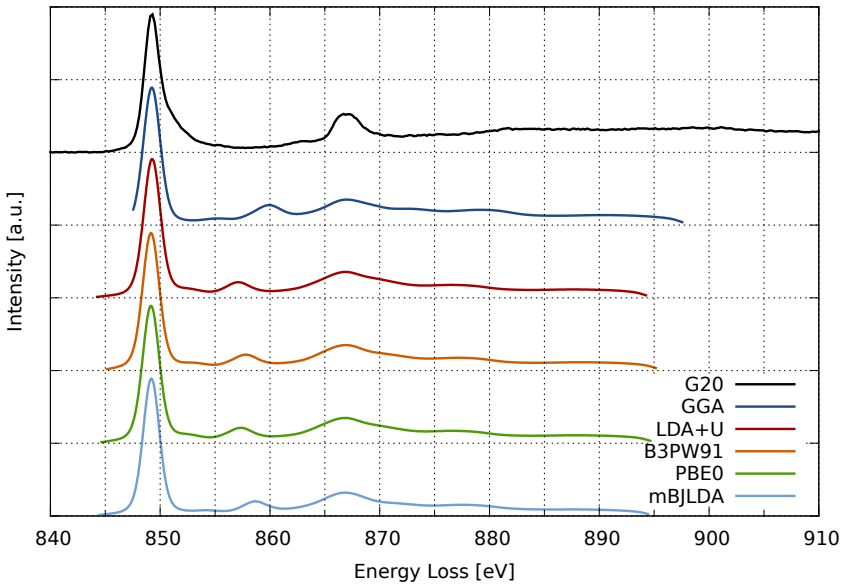

Figure 4.13.: Nickel $L_{2,3}$-edge ELNES calculated with different exchange-correlation functionals compared to an experimental spectrum.

of the Oxygen p-DOS calculated using the modified Becke-Johnson potential, the broadened and the unbroadened spectrum is shown in figure 4.12. This graph shows that the differences to the experimental spectrum at the peaks at 534 eV and 543 eV are due to the *broadening* program and the methods used therein.

A comparison of Ni $L_{2,3}$-ELNES calculated using different functionals and the experimental spectrum is shown in figure 4.13. As in the unit cell used for the WIEN2k simulation there are two different Nickel atoms, one spin-up and one spin-down, the ELNES for both atoms has to be calculated and summed up. There are only minor differences in the spectra calculated with different exchange-correlation functionals compared to the changes of the Oxygen K-ELNES. Only the position of the small second peak changes with different exchange-correlation functionals. Also the structure on the back of the L_3-peak, at about 850 eV, is changed by the usage of different functionals. In the experimental spectrum the second peak at 859 eV is not present. Also the background of the L_2-edge (above 870 eV) is much higher than in the numerical predictions. This leads to the suggestion that the Ni-DOS calculated using WIEN2k is not correct in every detail. This can be seen for example from figure 4.14, where the calculated L_3-edge and the corresponding partial DOS

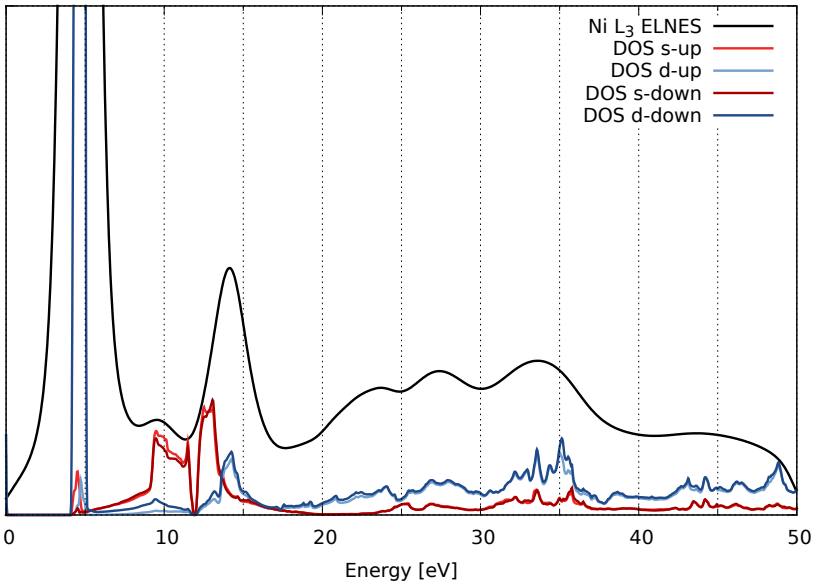

Figure 4.14.: Calculated Ni L_3-edge. The corresponding unoccupied partial DOS are superimposed.

are shown. It is clear that the structures of the unoccupied partial DOS at about 10 eV above Fermi-level give rise to the peak which is not present in the experimental spectrum. It is also evident from figure 4.13 that the calculated L_2-edge is broadened too much. This brings us back to the discussion, that the method used for calculating the broadening is not ideal and further investigations and improvements are necessary to describe the experimental data in every detail.

Summing up the results of the simulations, the choice of an appropriate exchange-correlation functional is crucial for the total DOS and the band gap, as well as the Oxygen K-ELNES. But choosing a different functional has almost no effect on the Ni $L_{2,3}$-ELNES.

4.3. Valence Electron Energy Loss Spectrometry

In [2] the optical band gap of NiO was calculated using different exchange-correlation functionals in WIEN2k and the Bethe-Salpeter equation. The calculated values were then compared to experimental values obtained by means of optical reflectivity measurements reported in [44]. The hybrid functionals reproduce the optical band

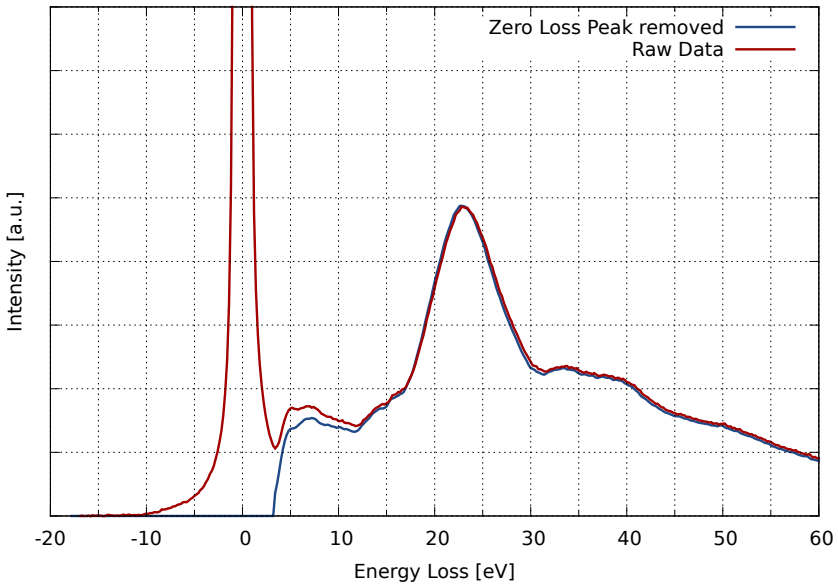

Figure 4.15.: Low voltage low loss EELS acquired at 40 kV. The deconvoluted spectrum is superimposed.

gap well, whereas the LDA+U funtional does not.

As outlined in [45] one can also determine the optical band gap as well as optical properties using valence electron energy loss spectrometry (VEELS). In order to avoid relativistic losses like Čerenkov losses, light guide modes and surface losses the VEELS measurements were performed using low voltage TEM, see [45–47] for details. The refractive index of NiO was reported in [44] to be 2.33. Therefore, according to [45] a high tension of 40 kV is sufficient to avoid relativistic losses. The low voltage VEELS measurements were perforem on a FEI TECNAI G^2 20 transmission electron microscope equipped with a LaB_6 cathode and a GATAN GIF 2001 energy filter. The spectra were recorded using a collection semi-angle of 2.8 mrad. The recorded low loss spectrum was deconvoluted using a separately recorded zero loss peak. In figure 4.15 the recorded spectrum as well as the deconvoluted one are shown. According to the low voltage VEELS a value of 3.0 eV for the optical band gap was determined, which can also be seen in this figure. This is in good agreement with the calculations in [2] as well as the optical reflectivity measurements in [44].

Furthermore, Kramers-Kronig analysis as described in [45] was performed to calculate optical properties of NiO. In figure 4.16 the resulting real and imaginary

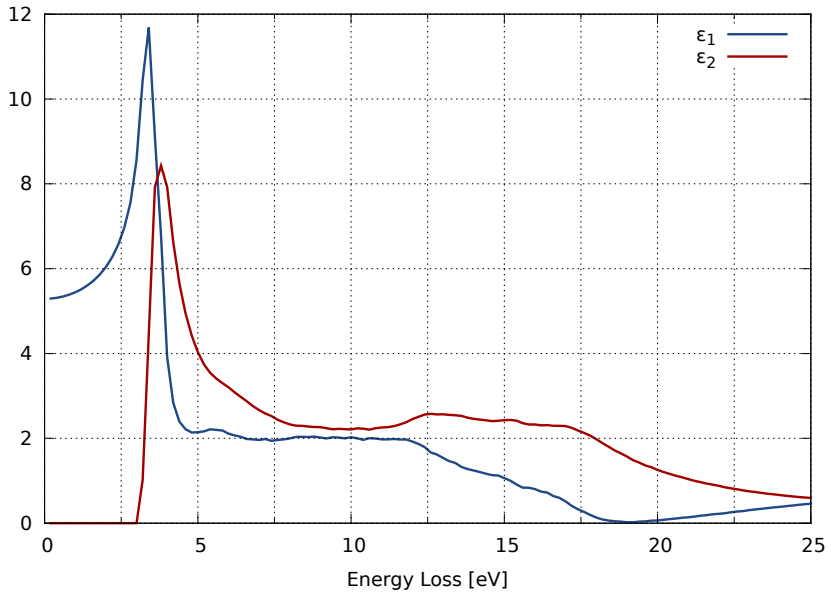

Figure 4.16.: Real and imaginary part of the complex dielectric function obtained by means of Kramers-Kronig analysis.

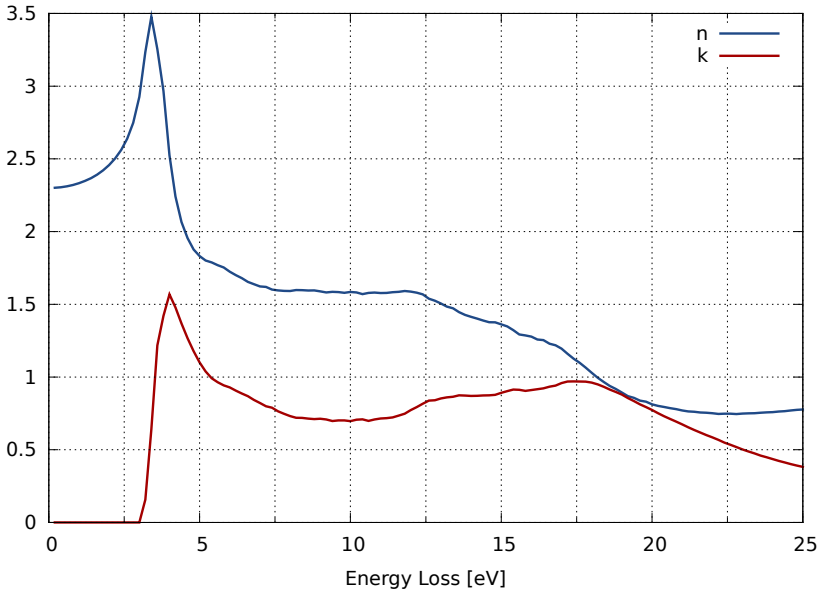

Figure 4.17.: Real and imaginary parts of the complex refractive index calculated using Kramers-Kronig analysis.

part of the complex dielectric function is shown. The calculated real and imaginary parts of the complex refractive index are shown in figure 4.17. The obtained functions are in good agreement with those determined in [44].

Part III.

Energy Loss by Channelled Electrons

5. Theoretical Background

5.1. Energy Loss by Channelled Electrons

In 1982 Taftø and Spence first used electron channelling in analytical TEM [7]. They called the technique *Atom Location by Channelling Enhanced Microanalysis* (ALCHEMI) [48] and used it to identify crystallographic sites and to analyse impurities. This is done by using the dependence of the characteristic X-ray emission on the orientation of the incident electron beam when doing energy dispersive X-Ray (EDX) analysis. Since these first experiments, ALCHEMI is commonly used in analytical microscopy. Soon after, electron channelling was also used in connection with EELS [6]. This technique is called *Energy Loss by Channelled Electrons* (ELCE) [49].

The principle of these techniques is simple. The electrons in the crystal can be described as Bloch-waves. Depending on the excitation error — and therefore on the orientation of the crystal with respect to the electron beam — these Bloch-waves have different weights. The Bloch-waves differ in the location of their intensity-maxima. If an atom coincides with these intensity maxima the energy-loss signal or X-ray signal originating from this site will be enhanced. In a simple picture, channelling conditions for the electron beam select site-specific chemical signals. The initial enthusiasm with ELCE faded away rapidly when it was realised that the situation is not that simple.

ALCHEMI is performed and interpreted easier than ELCE. This is because in ALCHEMI only the incoming electron wave has to be considered. For ELCE not only the incoming wave but also the outgoing electron wave as well as inelastic and elastic scattering processes have to be considered. As the spectrometer is usually placed off axis in ELCE-experiments, long acquisition-times are necessary and spectra often show a bad signal-to-noise ratio. Due to these theoretical and instrumental shortcomings, ELCE was not widely used until recent years [50].

Usually, measurements are performed under systematic-row conditions and not in

an ideal two-beam case. Therefore, predicting channelling behaviour is not straightforward any more and other effects, like interferometric EELS and sample thickness, have to be considered, see [51]. Thus, simulations have to be performed to find suitable detector positions that yield reasonable differences in EELS signal intensities.

In order to get an understanding of ELCE, in the next section a short overview of the important concepts of Bloch-waves and channelling is given. Afterwards, expressions of the DDSC, the dynamic form factor (DFF) and the mixed dynamic form factor (MDFF) are discussed.

5.2. Bloch-Waves and Channelling

For this short overview the derivations in [4] and [52] are followed. The Schrödinger equation for the crystal reads

$$\left[-\frac{\hbar^2}{2m_e}\nabla^2 + V(\boldsymbol{r})\right]\Psi(\boldsymbol{r}) = E\Psi(\boldsymbol{r})\,. \tag{5.1}$$

The potential inside a crystal is periodic:

$$V(\boldsymbol{r}) = V(\boldsymbol{r}+\boldsymbol{R})\,, \tag{5.2}$$

with $\boldsymbol{R}$ any lattice vector and $\boldsymbol{r}$ any vector in real space. Furthermore, the case of a centrosymmetric crystal is assumed, which gives, together with the fact that the potential must be real, the following condition:

$$V(\boldsymbol{r}) = V(-\boldsymbol{r}) = V^*(\boldsymbol{r})\,. \tag{5.3}$$

Now, the potential is written as a Fourier series

$$V(\boldsymbol{r}) = \sum_{\boldsymbol{g}} V_{\boldsymbol{g}} e^{i\boldsymbol{g}\cdot\boldsymbol{r}} = \frac{\hbar^2}{2m_e}\sum_{\boldsymbol{g}} U_{\boldsymbol{g}} e^{i\boldsymbol{g}\cdot\boldsymbol{r}}\,, \tag{5.4}$$

with $V_{\boldsymbol{g}} = \hbar^2/(2m_e)\cdot U_{\boldsymbol{g}}$ and the conditions (5.3) on $V(\boldsymbol{r})$ also hold for $U_{\boldsymbol{g}}$:

$$U_{\boldsymbol{g}} = U_{-\boldsymbol{g}} = U_{\boldsymbol{g}}^*\,. \tag{5.5}$$

The wave function $\Psi(\boldsymbol{r})$ is expanded into Bloch-waves $\psi^j(\boldsymbol{r})$ whose Bloch-functions $\mu^j(\boldsymbol{r})$ are again expanded into Fourier series:

$$\Psi(\boldsymbol{r}) = \sum_{j=1}^{n} \varepsilon^j \cdot \psi^j(\boldsymbol{r}) \tag{5.6}$$

$$\psi^j(\boldsymbol{r}) = \mu^j(\boldsymbol{r}) \cdot e^{i\boldsymbol{k}^j \cdot \boldsymbol{r}} \tag{5.7}$$

$$\mu^j(\boldsymbol{r}) = \sum_{\boldsymbol{g}} C^j_{\boldsymbol{g}} \cdot e^{i\boldsymbol{g} \cdot \boldsymbol{r}} \,. \tag{5.8}$$

The $\boldsymbol{g}$ are vectors in the reciprocal space and usually in TEM they are the diffraction vectors for the corresponding beams G. The Bloch-waves can then be written as

$$\psi^j(\boldsymbol{r}) = \sum_{\boldsymbol{g}} C^j_{\boldsymbol{g}} \cdot e^{i(\boldsymbol{k}^j + \boldsymbol{g}) \cdot \boldsymbol{r}} \,. \tag{5.9}$$

The superscript j denotes the dependence on a single value $\boldsymbol{k}^j$. Thus, each Bloch-wave $\psi^j(\boldsymbol{r})$ is a superposition of plane waves and the wave function $\Psi(\boldsymbol{r})$ is described in turn as a superposition of several Bloch-waves. ε^j is the excitation amplitude of the Bloch-wave j and is determined by the boundary conditions. In the work described in the following chapters, these boundary conditions demand that the incoming electron wave is a plane wave in the entrance plane of the crystal, while the outgoing wave is a plane wave in the exit plane of the crystal. The $C^j_{\boldsymbol{g}}$ are called the plane wave amplitudes.

Inserting the Fourier expansion of the potential (5.4) into the Schrödinger equation (5.1) yields a system of equations ($\forall j$)

$$\nabla^2 \psi^j(\boldsymbol{r}) + \left(\frac{2m_e}{\hbar^2} \cdot E + \sum_{\boldsymbol{g}} U_{\boldsymbol{g}} \cdot e^{i\boldsymbol{g} \cdot \boldsymbol{r}} \right) \psi^j(\boldsymbol{r}) = 0 \,. \tag{5.10}$$

The wave vector inside the crystal is defined as:

$$K^2 = \frac{2m_e E}{\hbar^2} + U_{\mathbf{0}} = k_0^2 + U_{\mathbf{0}} \,. \tag{5.11}$$

Inserting the Bloch-waves in the Schrödinger equation, together with the above definition, gives

$$\begin{aligned} 0 = &- \sum_{\boldsymbol{g}} C^j_{\boldsymbol{g}} \cdot \left(\boldsymbol{k}^j + \boldsymbol{g}\right)^2 \cdot e^{i(\boldsymbol{k}^j + \boldsymbol{g}) \cdot \boldsymbol{r}} \\ &+ K^2 \sum_{\boldsymbol{g}} C^j_{\boldsymbol{g}} \cdot e^{i(\boldsymbol{k}^j + \boldsymbol{g}) \cdot \boldsymbol{r}} + \sum_{\boldsymbol{h} \neq \boldsymbol{0}} U_{\boldsymbol{h}} \cdot e^{i\boldsymbol{h} \cdot \boldsymbol{r}} \cdot \sum_{\boldsymbol{g}} C^j_{\boldsymbol{g}} \cdot e^{i(\boldsymbol{k}^j + \boldsymbol{g}) \cdot \boldsymbol{r}} . \end{aligned} \tag{5.12}$$

Replacing $\boldsymbol{g}$ with $\boldsymbol{g} - \boldsymbol{h}$ in the last term of equation (5.12) yields

$$\sum_{\boldsymbol{g}} \left(\left[- \left(\boldsymbol{k}^j + \boldsymbol{g}\right)^2 + K^2 \right] \cdot C^j_{\boldsymbol{g}} + \sum_{\boldsymbol{h} \neq \boldsymbol{0}} U_{\boldsymbol{h}} C^j_{\boldsymbol{g}-\boldsymbol{h}} \right) \cdot e^{i\left(\boldsymbol{k}^j + \boldsymbol{g}\right) \cdot \boldsymbol{r}} = 0 . \tag{5.13}$$

As every coefficient of this equation must be zero separately one gets a series of equations (with again renaming $\boldsymbol{h}$ as $\boldsymbol{g} - \boldsymbol{h}$):

$$\left[K^2 - \left(\boldsymbol{k}^j + \boldsymbol{g}\right)^2 \right] \cdot C^j_{\boldsymbol{g}} + \sum_{\boldsymbol{h} \neq \boldsymbol{g}} U_{\boldsymbol{g}-\boldsymbol{h}} C^j_{\boldsymbol{h}} = 0 . \tag{5.14}$$

This set of equations can be written as a matrix equation

$$\boldsymbol{A} \cdot \boldsymbol{C} = \boldsymbol{0} , \tag{5.15}$$

with the vector

$$\boldsymbol{C} = \begin{pmatrix} C^j_{\boldsymbol{0}} \\ C^j_{\boldsymbol{g}_1} \\ C^j_{\boldsymbol{g}_2} \\ \vdots \end{pmatrix} . \tag{5.16}$$

The matrix $\boldsymbol{A}$ is defined by its diagonal elements

$$a_{gg} = K^2 - \left(\boldsymbol{k}^j + \boldsymbol{g}\right)^2 \tag{5.17}$$

and off-diagonal elements

$$a_{gh} = U_{\boldsymbol{g}-\boldsymbol{h}} . \tag{5.18}$$

According to [52] it is assumed that $\boldsymbol{k}^j$ differs from $\boldsymbol{K}$ in z-direction by a small amount γ^j such, that

$$\boldsymbol{k}^j = k_x^j \boldsymbol{e}_x + k_y^j \boldsymbol{e}_y + k_z^j \boldsymbol{e}_z = K_x^j \boldsymbol{e}_x + K_y^j \boldsymbol{e}_y + \left(K_z^j + \gamma^j\right) \boldsymbol{e}_z \,. \tag{5.19}$$

Furthermore, if the electron beam is tilted with respect to the crystal, k_x depends on the tilt angle θ and excitation error $\boldsymbol{s_g}$ by

$$\theta = k_x / K = s_{\boldsymbol{g}} / g \,. \tag{5.20}$$

By inserting this into equation (5.14) one gets the matrix equation

$$\boldsymbol{A} \cdot \boldsymbol{C} = \gamma^j \boldsymbol{C} \,, \tag{5.21}$$

which is an eigenvalue problem with the eigenvalues γ^j and corresponding eigenvectors $C_{\boldsymbol{g}}^j$. The matrix elements are now

$$A_{11} = 0,\; A_{gg} = s_{\boldsymbol{g}},\; A_{gh} = U_{\boldsymbol{g}-\boldsymbol{h}}/(2K) \,. \tag{5.22}$$

For more details on the Bloch-wave formalism see [4, 51, 52].

5.3. Inelastic Scattering

According to Fermi's golden rule, the transition rate from an initial state $|\Psi_i\rangle$ to a final state $|\Psi_f\rangle$ reads

$$W_{i\to f} = \frac{2\pi}{\hbar} \left| \left\langle \Psi_f \middle| \hat{V} \middle| \Psi_i \right\rangle \right|^2 k_f \frac{m_e}{\hbar^2} dE d\Omega \cdot \delta\left(E_{|\Psi_f\rangle} - E_{|\Psi_i\rangle}\right) \,, \tag{5.23}$$

where $k_f \frac{m}{\hbar^2} dE d\Omega$ represents a phase space element around $|\Psi_f\rangle$. The total system is initially in the state

$$|\Psi_i\rangle = |\psi_i\rangle \otimes |i\rangle \tag{5.24}$$

and the final state is

$$|\Psi_f\rangle = |\psi_f\rangle \otimes |f\rangle \,, \tag{5.25}$$

with $|\psi_{i,f}\rangle$ the state of the probe electron and $|i\rangle$,$|f\rangle$ the states of the target system. The energy loss E of the probe is then given by $E = E_{|f\rangle} - E_{|i\rangle}$. Thus, the transition rate is

$$W_{i\to f} = \frac{2\pi}{\hbar}\sum_i p_i \sum_f \left|\left\langle \psi_f \left| \left\langle f \left| \hat{V} \right| i \right\rangle \right| \psi_i \right\rangle\right|^2 k_f \frac{m_e}{\hbar^2} dE d\Omega \cdot \delta\left(E_{|f\rangle} - E_{|i\rangle} - E\right) , \tag{5.26}$$

with p_i the occupation probability of the target's initial states.

For discussion of the DDSC the probe states are described as plane waves[1]:

$$|\psi\rangle = |k\rangle = \frac{1}{(2\pi)^{3/2}} e^{i\boldsymbol{k}\cdot\boldsymbol{r}} . \tag{5.27}$$

Considering the Born-Oppenheimer approximation and the one-electron approximation (see [51]), only the Coulomb interaction of the probe electron at $\boldsymbol{r}$ and the target electron at $\boldsymbol{R}$ has to be taken into account:

$$V(\boldsymbol{r}-\boldsymbol{R}) = \frac{e^2}{4\pi\epsilon_0}\cdot\frac{1}{|\boldsymbol{r}-\boldsymbol{R}|} . \tag{5.28}$$

When making use of the shift theorem for Fourier transformations [53], the integral $\langle k_f \,|\, V(\boldsymbol{r}-\boldsymbol{R}) \,|\, k_i\rangle$ yields

$$\begin{aligned}
\langle k_f \,|\, V(\boldsymbol{r}-\boldsymbol{R}) \,|\, k_i\rangle &= \frac{e^2}{4\pi\epsilon_0}\cdot\frac{1}{(2\pi)^3}\cdot\int d^3r e^{-i\boldsymbol{k}_f\cdot\boldsymbol{r}}\frac{1}{|\boldsymbol{r}-\boldsymbol{R}|}e^{i\boldsymbol{k}_i\cdot\boldsymbol{r}} \\
&= \frac{e^2}{4\pi\epsilon_0}\cdot\frac{1}{(2\pi)^3}\cdot\int d^3r e^{i\boldsymbol{Q}\cdot\boldsymbol{r}}\frac{1}{|\boldsymbol{r}-\boldsymbol{R}|} \\
&= \frac{e^2}{4\pi\epsilon_0}\cdot\frac{1}{(2\pi)^3}\cdot\frac{4\pi}{Q^2}e^{i\boldsymbol{Q}\cdot\boldsymbol{R}} \\
&= \frac{e^2}{(2\pi)^3\epsilon_0}\cdot\frac{1}{Q^2}\cdot e^{i\boldsymbol{Q}\cdot\boldsymbol{R}} ,
\end{aligned} \tag{5.29}$$

with the scattering vector

$$\boldsymbol{Q} = \boldsymbol{k}_i - \boldsymbol{k}_f . \tag{5.30}$$

The scattering vector consists of the lateral momentum transfer $\boldsymbol{q} = (q_x, q_y)$ and the

[1] Note that every arbitrary wave-form can be expanded into a set of plane waves.

characteristic momentum transfer for inelastic scattering q_E:

$$\boldsymbol{Q} = \begin{pmatrix} q_x \\ q_y \\ q_E \end{pmatrix} . \tag{5.31}$$

The characteristic momentum transfer is defined as [54]

$$q_E = k_0 \frac{E}{E_0} \left(\frac{E_0 + m_e c^2}{E_0 + 2 m_e c^2} \right) , \tag{5.32}$$

with the wave vector of the incoming electron beam k_0, depending on the definition of a reciprocal vector, either $k_0 = (2\pi)/\lambda$ or $k_0 = 1/\lambda$. In order to be able to compare q_E with the acquired diffraction patterns shown in section 7.1, the definition $k_0 = 1/\lambda$ is used. As all the measurements and simulations are done with an electron beam voltage of 200 kV, the corresponding value of k_0 is $k_0 = 399\ \mathrm{nm}^{-1}$. The characteristic momentum transfer for the O K-edge at 530 eV is then $q_E = 0.61\ \mathrm{nm}^{-1}$, while for the Ni $L_{2,3}$-edge at 855 eV it is $q_E = 0.99\ \mathrm{nm}^{-1}$.

Similar to the derivations in [51], the initial probe state for interferometric EELS is taken as a superposition of two plane waves

$$|k_i\rangle = a_1 |k_1\rangle + a_2 |k_2\rangle , \quad |a_1|^2 + |a_2|^2 = 1 , \tag{5.33}$$

while the final probe state is still a single plane wave $|k_f\rangle$.

Inserting equations (5.28), (5.29) and (5.33) into equation (5.26) yields:

$$\begin{aligned} W_{i\to f} = \frac{2\pi}{\hbar} k_f \frac{m_E}{\hbar^2} dE d\Omega \left(\frac{e^2}{(2\pi)^3 \epsilon_0} \right)^2 \\ \times \Bigg[|a_1|^2 \frac{1}{Q^4} \sum_i p_i \sum_f \left| \langle f | e^{i \boldsymbol{Q} \cdot \boldsymbol{R}} | i \rangle \right|^2 \\ + |a_2|^2 \frac{1}{Q'^4} \sum_i p_i \sum_f \left| \langle f | e^{i \boldsymbol{Q'} \cdot \boldsymbol{R}} | i \rangle \right|^2 \\ + 2\Re \left[a_1 a_2^* \frac{1}{Q^2 Q'^2} \sum_i p_i \sum_f \langle f | e^{i \boldsymbol{Q} \cdot \boldsymbol{R}} | i \rangle \langle i | e^{-i \boldsymbol{Q'} \cdot \boldsymbol{R}} | f \rangle \right] \Bigg] \\ \times \delta \left(E_f - E_i - E \right) , \end{aligned} \tag{5.34}$$

with the momentum transfers

$$\boldsymbol{Q} = \boldsymbol{k}_1 - \boldsymbol{k}_f \tag{5.35}$$

$$\boldsymbol{Q}' = \boldsymbol{k}_2 - \boldsymbol{k}_f \,. \tag{5.36}$$

Now one can introduce the dynamic form factor (DFF) and the mixed dynamic form factor (MDFF). The DFF reads

$$S(\boldsymbol{Q}, E) = \sum_i p_i \sum_f \left| \left\langle f \,\middle|\, e^{i\boldsymbol{Q}\cdot\boldsymbol{R}} \,\middle|\, i \right\rangle \right|^2 \cdot \delta(E_f - E_i - E) \,, \tag{5.37}$$

while the MDFF reads

$$S(\boldsymbol{Q}, \boldsymbol{Q}', E) = \sum_i p_i \sum_f \langle f | e^{i\boldsymbol{Q}\cdot\boldsymbol{R}} | i \rangle \, \langle i | e^{i\boldsymbol{Q}'\cdot\boldsymbol{R}} | f \rangle \cdot \delta(E_f - E_i - E) \,. \tag{5.38}$$

One can also get the DFF out of the MDFF by setting $\boldsymbol{Q} = \boldsymbol{Q}'$, thus $S(\boldsymbol{Q}, E) = S(\boldsymbol{Q}, \boldsymbol{Q}, E)$. By inserting these definitions in equation (5.34) and using the relation

$$d\sigma(\Omega, E) = W_{i\to f} (2\pi)^3 \frac{m_e}{\hbar k_i} \,, \tag{5.39}$$

the double differential scattering cross section is found to be

$$\begin{aligned} \frac{\partial\sigma}{\partial E \partial\Omega} = \frac{2\pi}{\hbar} k_f \frac{m_e}{\hbar^2} \left(\frac{e^2}{(2\pi)^3 \epsilon_0} \right)^2 (2\pi)^3 \frac{m_e}{\hbar k_i} \\ \times \Bigg[|a_1|^2 \frac{1}{Q^4} S(\boldsymbol{Q}, E) + |a_2|^2 \frac{1}{Q'^4} S(\boldsymbol{Q}', E) \\ + 2\Re \left[a_1 a_2^* \frac{1}{Q^2 Q'^2} S(\boldsymbol{Q}, \boldsymbol{Q}', E) \right] \Bigg] \,. \end{aligned} \tag{5.40}$$

Using the definition of the Bohr radius $a_0 = (4\pi\epsilon_0\hbar^2)/(m_e e^2)$ and considering relativistic corrections by $m_e \to \gamma m_e$, this simplifies to

$$\begin{aligned} \frac{\partial\sigma}{\partial E \partial\Omega} = \frac{4\gamma^2}{a_0^2} \cdot \frac{k_f}{k_i} \Bigg[|a_1|^2 \frac{1}{Q^4} S(\boldsymbol{Q}, E) + |a_2|^2 \frac{1}{Q'^4} S(\boldsymbol{Q}', E) \\ + 2\Re \left[a_1 a_2^* \frac{1}{Q^2 Q'^2} S(\boldsymbol{Q}, \boldsymbol{Q}', E) \right] \Bigg] \,. \end{aligned} \tag{5.41}$$

The calculation of $S(\boldsymbol{Q},\boldsymbol{Q}',E)$ for crystalline environments is done in [51] where different expressions for the MDFF are derived. In chapter 3 of [51] a general expression as well as an expression involving the unoccupied partial DOS is given, which is used in the program *TELNES.2* of the WIEN2k simulation package (see section 3.4.2). In chapter 4 of [51] the MDFF is calculated for a Bloch-wave representation of the incoming and outgoing electron waves. The DDSC reads then

$$\frac{\partial\sigma}{\partial E\partial\Omega} = \frac{4\gamma^2}{a_0^2}\frac{k_f}{k_i}\sum_{\substack{j,j',l,l'\\ \boldsymbol{g},\boldsymbol{g}',\boldsymbol{h},\boldsymbol{h}'}} \varepsilon_j C^j_{\boldsymbol{g}}(\tilde{\varepsilon}_l\tilde{C}^l_{\boldsymbol{h}})^*(\varepsilon_{j'}C^{j'}_{\boldsymbol{g}'})^*\tilde{\varepsilon}_{l'}\tilde{C}^{l'}_{\boldsymbol{h}'}\cdot e^{2\pi(\boldsymbol{Q}-\boldsymbol{Q}')\cdot\boldsymbol{X}}\cdot e^{2\pi id(\tilde{\gamma}_{l'}-\tilde{\gamma}_l)} \times\frac{S(\boldsymbol{Q},\boldsymbol{Q}',E)}{Q^2Q'^2}\,, \tag{5.42}$$

where all the variables with a tilde describe the outgoing electron wave, while all the variables without tilde describe the incoming wave. Equation (5.42) is a generalisation of equation (5.41) and it is the basis equation for the simulation program with which the calculations in this part of the work were performed. This program is described in [55], where also more details on equation (5.42) and its implementation in the software package are given.

In equation (5.42) the dipole approximation of the MDFF is used, which yields

$$\Re\left[S(\boldsymbol{Q},\boldsymbol{Q}',E)\right] \propto (\boldsymbol{Q}\cdot\boldsymbol{Q}') \tag{5.43}$$

$$\Im\left[S(\boldsymbol{Q},\boldsymbol{Q}',E)\right] \propto (\boldsymbol{Q}\times\boldsymbol{Q}')\cdot\frac{\boldsymbol{M}}{M}\,, \tag{5.44}$$

with $\boldsymbol{M}$ the net magnetic moment of the scattering atom (see [56]).[2] With this the MDFF reads:

$$S(\boldsymbol{Q},\boldsymbol{Q}',E) = f(E)\cdot(\boldsymbol{Q}\cdot\boldsymbol{Q}') + i\cdot g(E)\cdot(\boldsymbol{Q}\times\boldsymbol{Q}')\cdot\boldsymbol{e_B}\,, \tag{5.45}$$

with $f(E)$ and $g(E)$ as functions of the energy loss only.[3]

In the experiments reported in section 7.1 NiO is investigated in [1 1 0] zone-axis with systematic-row condition including the $(\bar{1}\,1\,1)$ reflex. In this configuration, each

[2] Usually the magnetic moment is forced to be parallel to the optical axis of the TEM by the magnetic field (≈ 2 T) of the objective lenses. Thus, $\boldsymbol{M}/M = \boldsymbol{e_B}$.

[3] The exact form of $f(E)$ and $g(E)$ depend on $|i\rangle$ and $|f\rangle$ of the scattering centre, of course. Thus, they are different for different atomic species and also for K-, L_2-, L_3-, ... edges. In the used approximation and for one atom–edge combination they are only a function of E, however.

atomic column contains Ni atoms with alternating spins. Thus, the average magnetic contribution can be neglected. Therefore, in the following, only the real part of the dipole approximation is considered. The MDFF then reads

$$S(\boldsymbol{Q}, \boldsymbol{Q}', E) = f(E) \cdot (\boldsymbol{Q} \cdot \boldsymbol{Q}') \,. \tag{5.46}$$

As mentioned above, when doing ELCE experiments, not only channelling conditions have to be observed. Due to the placement of the EELS detector off the diffraction spots, also the behaviour of the MDFF cannot be neglected. The effects of channelling and antichannelling conditions can be reversed, depending on the position of the EELS detector. This is described shortly in [51]. Moreover, due to the Lorentzian shape of the DDSC, the intensity decreases very fast as the detector is moved further away from the diffraction spots. For the sake of sample stability and to decrease acquisition times, the detector should therefore not be placed too far away from the diffraction spots. Considering all these effects, simulations of the experimental configuration are necessary, which are described in the next chapter.

6. Simulations

The simulation program used in this work is described in [55]. The program is written in object-oriented C++ code and takes its input parameters from an extensible markup language (XML) configuration file. The output is plain-text based.

The configuration file is divided into different sections. First the output files are specified and the crystal parameters as well as the atom positions are defined. The crystallographic data given in table 6.1 was used for the conducted calculations. As microscope specific parameters the acceleration voltage and the limiting aperture in the diffraction plane enter. Then the experimental setup is described. This is done by specifying the zone axis, the surface normal, the position of the Laue circle centre and the position of the detectors relative to the transmitted unscattered beam. Furthermore, the model for the calculation of the MDFF has to be given. For the performed simulations the simple dipole model from equation (5.46) was used.

Finally required data for the specific calculation has to be defined. There are three possible calculation modes implemented in the program: *bloch-wave maps*, *xz-maps* and *thickness maps*. The different modes as well as the corresponding calculation results are reported in the following sections.

6.1. Bloch-Wave Maps

As input data for calculating Bloch-wave maps the x and z ranges has to be given. In this calculation mode the program computes the Bloch-waves inside the crystal. Using the input data the excitation of the different diffraction spots is determined. With this, the possible Bloch-waves and their excitations are calculated. In the output file the Bloch-wave intensities with respect to the coordinates inside the given crystal are written. Usually a xz-coordinate system is used to plot the intensities. The program assumes that the intensity is 1 at every point of the entrance plane. Then it calculates how this intensity changes inside the crystal. In figure 6.1 a sketch of the incident

Lattice parameters	Atom	Atom positions
a = b = c = 0.417 nm	Ni	$x = 0,\ y = 0,\ z = 0$
$\alpha = \beta = \gamma = 90°$		$x = 0.5,\ y = 0.5,\ z = 0$
		$x = 0.5,\ y = 0,\ z = 0.5$
		$x = 0,\ y = 0.5,\ z = 0.5$
	O	$x = 0.5,\ y = 0.5,\ z = 0.5$
		$x = 0.5,\ y = 0,\ z = 0$
		$x = 0,\ y = 0.5,\ z = 0$
		$x = 0,\ y = 0,\ z = 0.5$

Table 6.1.: Input data for calculation of NiO. Atom positions are given in local coordinates of the unit cell.

beam geometry is shown and the intensities for exact channelling conditions inside the NiO crystal are plotted. For this calculation a value of $(\overline{6}\,6\,12)$ for the position of the Laue circle centre and [1 1 0] for the zone axis were used. This calculation resembles a possible incoming electron wave when doing ELCE-experiments. It can be seen that the intensity maxima lie in the rows of Ni atoms. Furthermore, oscillations of the intensity in the z-coordinate can be seen. This is related to the so-called "Pendellösung" (see [4, 52]).

In figure 6.2 a sketch of the incident beam geometry is shown and the Bloch-wave intensities are plotted when using $(\overline{5.9}\,5.9\,12.7)$ as position of the Laue circle centre. Due to the reciprocity theorem [57] this resembles a possible outgoing electron wave in an ELCE-experiment. It is evident from this figure that the intensity maxima of the outgoing Bloch-waves are not parallel to the atomic columns any more. Instead they point towards the position of the detector.

6.2. XZ Maps

For this type of calculations again the x and z ranges have to be given. Additionally the sort of atoms and the corresponding energy loss for the calculation of the inelastic scattering process are taken as input data. In the xz-map calculation mode the program determines the incoming and outgoing Bloch-waves as described in section 6.1. With this, the DDSC is calculated according to equation (5.42). The result is a kind of hypothetical "Intensity map" which shows how much a specific position inside the

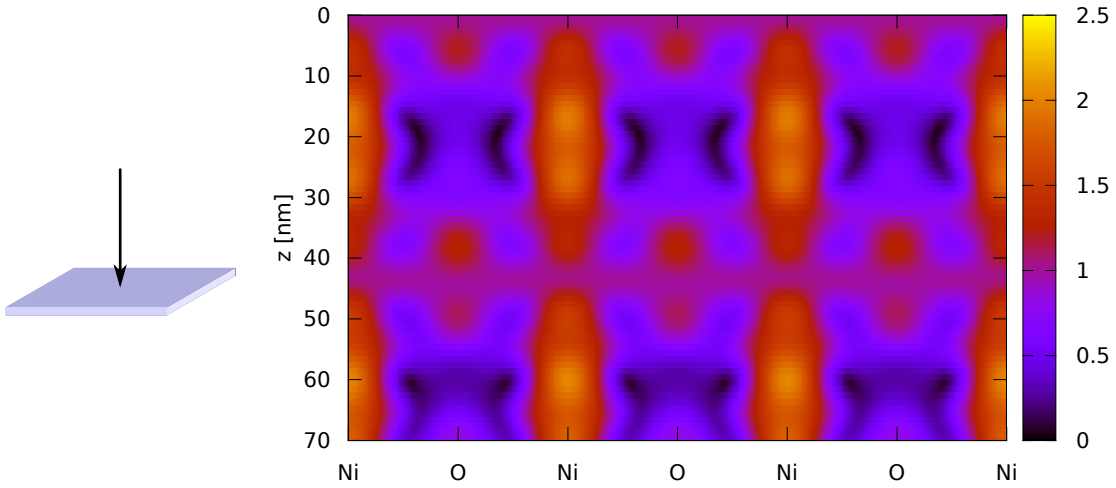

Figure 6.1.: Sketch of the incident beam geometry and plot of the calculated intensities of Bloch-waves resembling an incoming electron wave inside the crystal. Intensities are printed from low (black) to high (yellow).

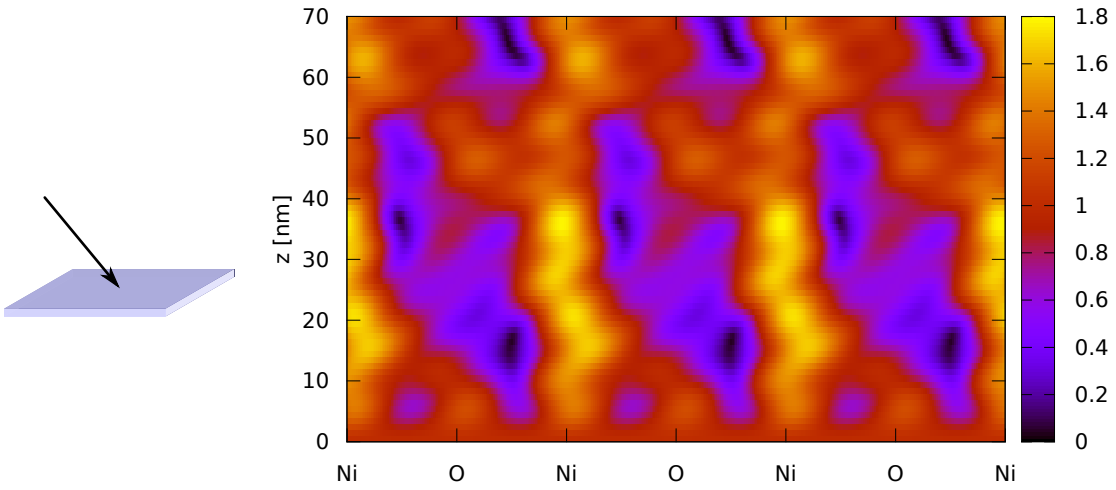

Figure 6.2.: Sketch of the incident beam geometry and plot of the calculated intensities of Bloch-waves resembling an outgoing electron wave inside the crystal. Intensities are printed from low (black) to high (yellow).

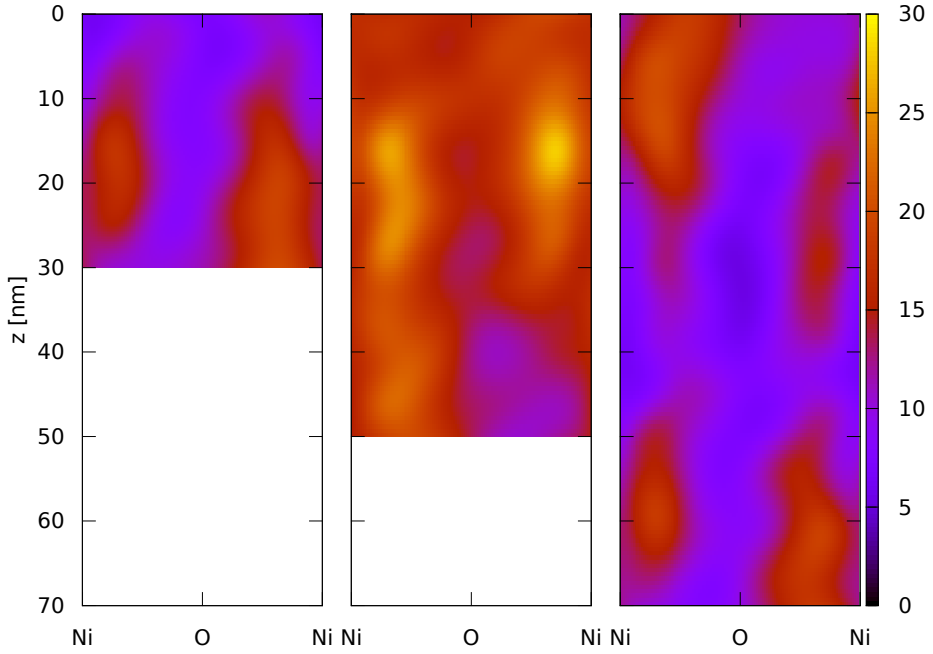

Figure 6.3.: Calculated intensities of inelastic scattering plotted for three different sample thicknesses. Intensities are printed from low (black) to high (yellow).

crystal contributes to the inelastic scattering signal assuming a proper scattering centre is placed there. As the Bloch-waves depend on the crystal thickness, the resulting xz-maps show strong differences for different sample thicknesses. As an example the xz-maps for inelastic scattering at the O K-edge at 530 eV for different crystal thicknesses are shown in figure 6.3.

6.3. Thickness Maps

For generating thickness-maps one can think of the simulation program performing several steps. First, the contributions to the DDSC for a specific scattering process with corresponding energy loss are calculated as mentioned is section 6.2. The contributions at the positions of the specified sort of atoms are then summed up. This is done for each thickness in the interval specified in the input file. The results are then written into an output file such that the resulting signal intensity for this specific scattering process can be plotted with respect to the sample thickness. As

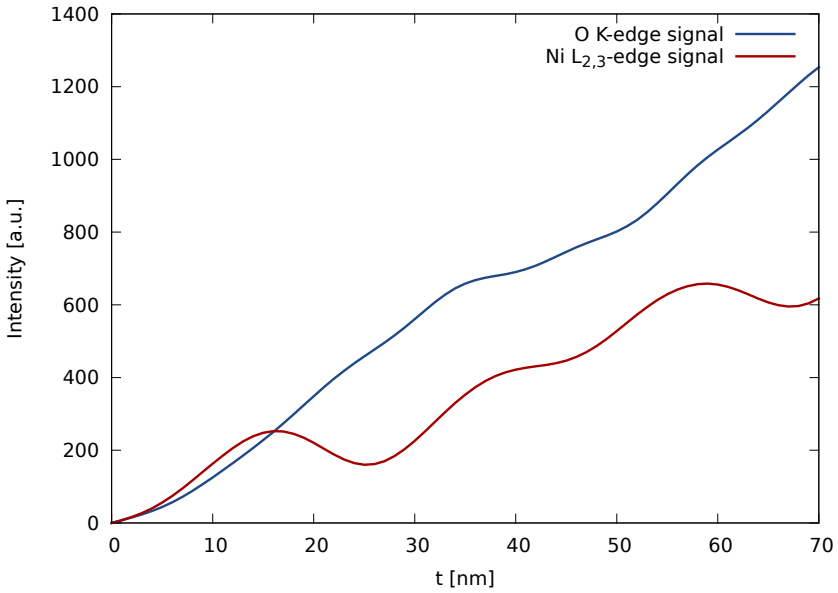

Figure 6.4.: Calculated signal intensities for the O K-edge and the Ni $L_{2,3}$-edge with respect to the sample thickness t.

an example the resulting signal intensity for the O K-edge at 530 eV as well as the intensity for the Ni $L_{2,3}$-edge at 855 eV are shown in figure 6.4. The detector position was set to $(1.12\,\overline{1.12}\,1.97)$. In the original ELCE-experiments reported by Taftø and Krivanek [6], the differences in the relative signal intensities at different channelling conditions are of interest. The different channelling conditions were established by tilting the sample. According to the reciprocity theorem [58], one can also shift the EELS detector in the diffraction pattern which is equivalent to tilting the outgoing beam. This also changes the channelling conditions inside the crystal. Thus, in figure 6.5 the ratios of the O K-edge and Ni $L_{2,3}$-edge signal intensities are plotted for different detector positions. For convenience a coordinate system for placing the EELS detector was defined such that one axis (referred to as η) is parallel to the systematic row, while the second axis (referred to as κ) is perpendicular to it. The unit length is defined as the distance between the $\mathbf{0}$ and $\boldsymbol{G}$-beams which is the closest allowed reciprocal lattice vector. In this coordinate system the detector positions were taken to be $(\eta, \kappa) = (0.4, 0.4)$, $(0.6, 0.4)$, $(1.4, 0.4)$ and $(1.6, 0.4)$. It is evident that the differences in relative signal intensities strongly depend on sample thickness. Also different detector positions have a great influence on the relative

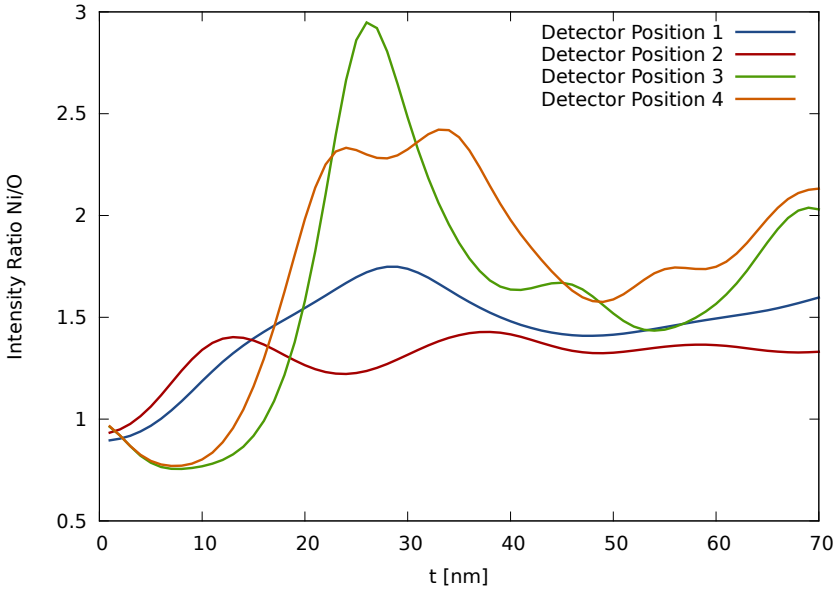

Figure 6.5.: Ratio of the Ni $L_{2,3}$-edge and the O K-edge plotted for the detector positions $(\eta, \kappa) = (0.4, 0.4)$, $(0.6, 0.4)$, $(1.4, 0.4)$ and $(1.6, 0.4)$ with respect to the sample thickness t.

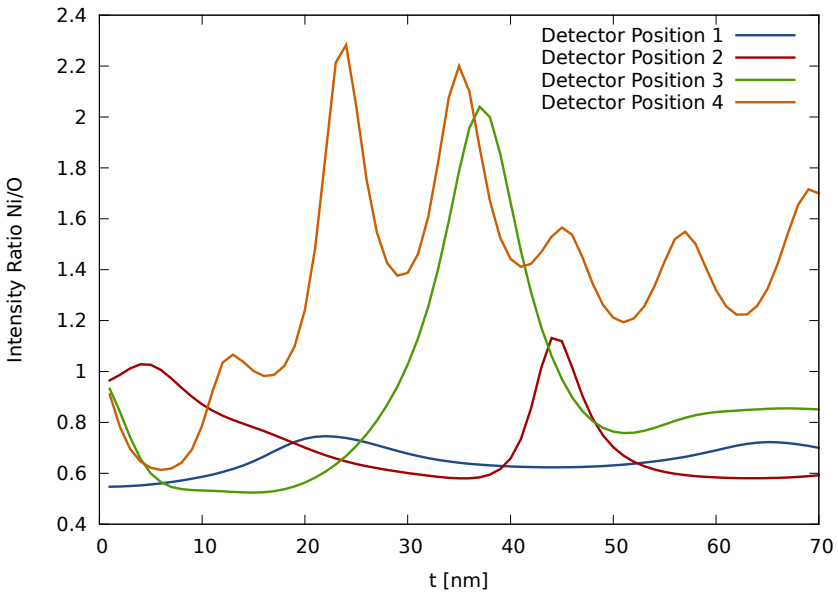

Figure 6.6.: Ratio of the Ni $L_{2,3}$-edge and the O K-edge plotted for the detector positions $(\eta, \kappa) = (0.1, 0.1)$, $(0.9, 0.1)$, $(1.1, 0.1)$ and $(1.9, 0.1)$ with respect to the sample thickness t.

signal intensities. As a comparison, in figure 6.6 the same diagram is shown for the different detector positions $(\eta, \kappa) = (0.1, 0.1)$, $(0.9, 0.1)$, $(1.1, 0.1)$ and $(1.9, 0.1)$. From these two figures it is clear that performing ELCE-experiments is not straightforward and that supporting simulations are essential for interpreting the results.

7. Experiments and Interpretation

7.1. Measurements

The following experiments were performed using a FEI TECNAI G^2 F20 (from now on referred to as F20) with a field emission gun (FEG) and equipped with a GATAN GIF Tridiem energy filter and on a FEI TECNAI G^2 20 (from now on referred to as G20) with a LaB_6 cathode and equipped with a GATAN GIF 2001 energy filter. Both instruments were operated at 200 kV acceleration voltage.

As mentioned in the previous section, in the original ELCE-experiments [6] different channelling conditions were established by tilting the sample. As tilting cannot be performed with high precision easily in the used instruments, shifting of the EELS detector could be used instead. As the post-column energy filter is fixed, this is performed by shifting the diffraction pattern. This is done with high precision using a Digital Micrograph script. For this purpose a coordinate system (η, κ) with one axis parallel to the systematic row and one perpendicular to it was defined as described in section (6.3). In the script the unit length is defined as the distance between the **0** beam and the $\boldsymbol{G}$ beam. This is calibrated by aligning the corresponding diffraction spots with the spectrometer entrance aperture (SEA). This alignment is shown in figure 7.1. The script is able to shift the diffraction pattern with high precision into any position given in the new coordinate system. From now on, when writing about placing the EELS detector somewhere in the diffraction pattern, a shift of the diffraction pattern with respect to the SEA is meant.

As the EELS measurements are performed off axis (a certain distance away from the diffraction spots), intensity decreases very fast when placing the detector further away from the spots due to the Lorentzian behaviour of the DFF. In order to increase intensity, the diffraction spots are spread such that the spot corresponding to the **0** beam fills out the SEA which is equivalent to choosing the convergence semi-angle

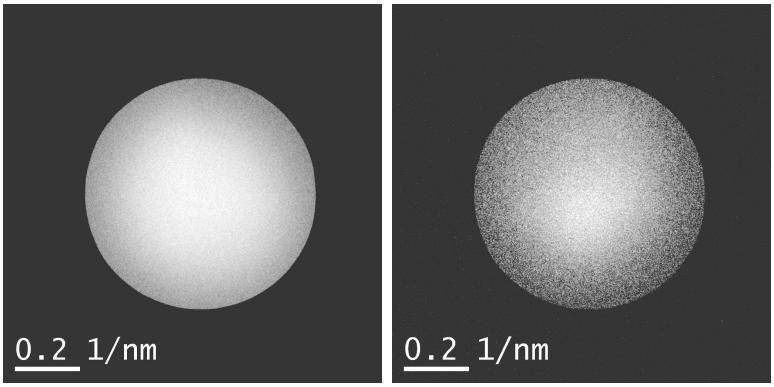

Figure 7.1.: Image of the **0** beam (left) and the $\boldsymbol{G}$ beam (right). The SEA is visible as circular aperture limiting momentum transfers to $|\boldsymbol{q}| \leq 0.35\ \mathrm{nm}^{-1}$. This corresponds to a collection semi-angle $\beta = 0.9$ mrad.

similar to the collection semi-angle $\alpha \approx \beta$. This can be seen from figure 7.1.

The following measurements were conducted on the G20. A bright field (BF) image of the investigated area of the specimen is shown in figure 7.2. The specimen was tilted out of the [1 1 0] zone axis to obtain a systematic row condition including the $(\bar{1}\,1\,1)$ diffraction spot. The corresponding diffraction pattern is shown in figure 7.3.

The thickness was measured using the Log-ratio method [54]. In order to do so, a low loss spectrum was acquired which is shown in figure 7.4. The obtained thickness was 12 nm. As a rule of thumb, the real thickness is estimated to be in an interval of ±2 nm of the calculated value. From the FWHM of the zero loss peak the experimental broadening was determined to be 1.5 eV.

EELS measurements were performed at the detector positions $(\eta, \kappa) = (0.3, 0.3)$, $(0.7, 0.3)$ and $(1.3, 0.3)$. A sketch of the experimental setup is shown in figure 7.5. As described in section 6 the specimen thickness is crucial for ELCE-experiments. Due to the specimen preparation the thickness changes rapidly when moving away from the hole in the specimen centre. Therefore, a selected area aperture (SAA) was used in order to restrict thickness changes of the investigated specimen area. The effective size of the SAA back-projected to the objective plane is 200 nm. A SEA of 2 mm diameter corresponding to a collection semi-angle $\beta = 0.9$ mrad and a disperson of 0.5 eV per pixel were chosen such that the O K-edge and the Ni $L_{2,3}$-edge could be acquired simultaneously in the same spectrum. The acquisition time was 240 s for each measurement. A background subtraction using a power-law fit [54] was

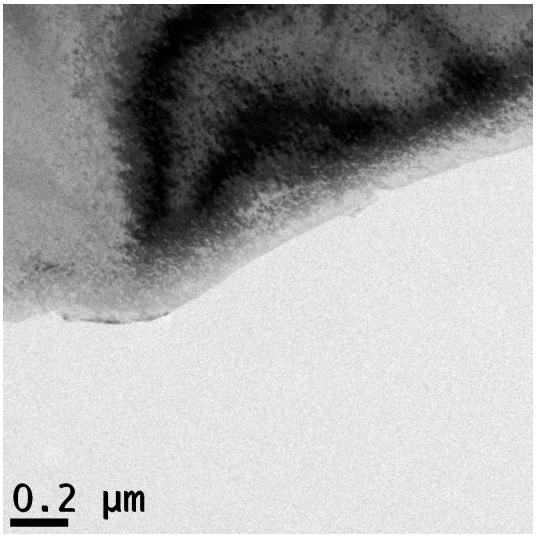

Figure 7.2.: Bright field image of the investigated sample area.

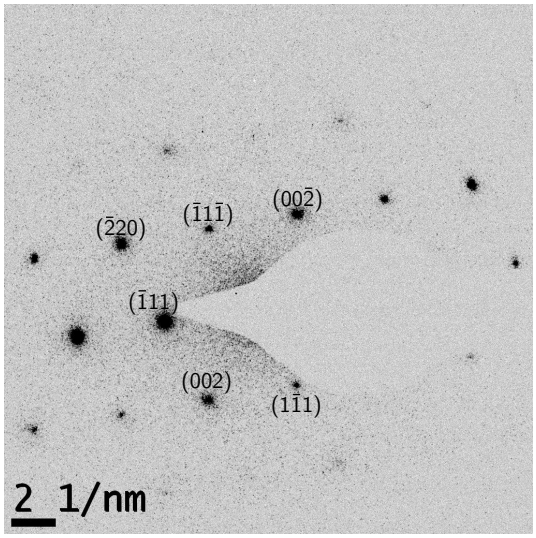

Figure 7.3.: Diffraction pattern of NiO in systematic row condition including the $(\bar{1}\,1\,1)$ diffraction spot. Due to the close proximity to the systematic row, adjacent diffraction spots show up as well.

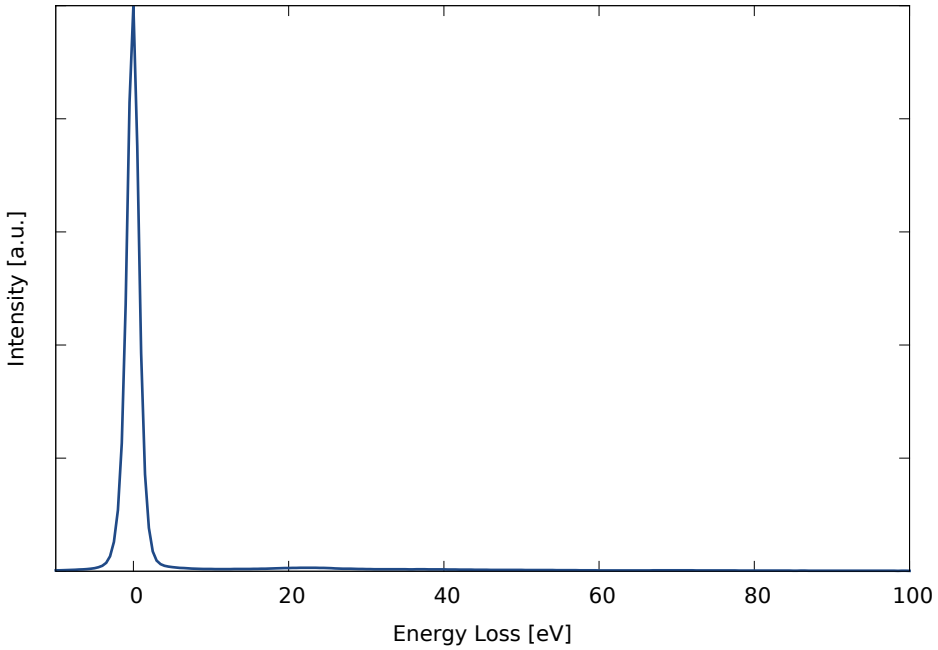

Figure 7.4.: Low loss spectrum of NiO acquired on the G20 at a typical measurement position. Note that the plasmon around 22 eV is barely visible indicating a very thin specimen. The Log-ratio method yields a thickness of 12 nm.

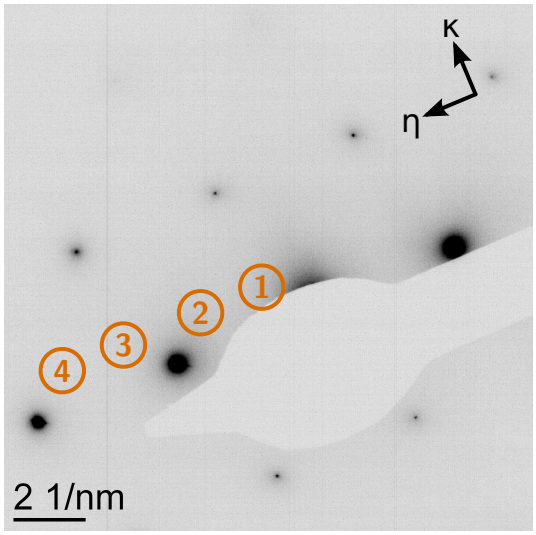

Figure 7.5.: Sketch of the experimental setup. The different detector positions are labelled with 1 to 4. Furthermore, the axes of the used coordinate system are shown.

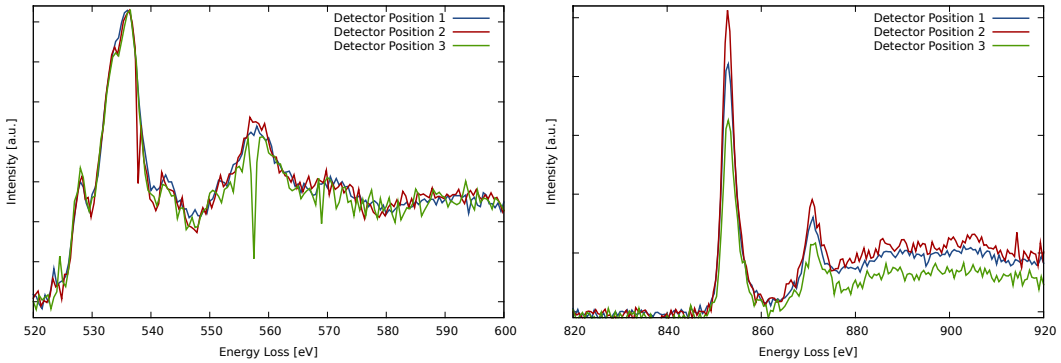

Figure 7.6.: Acquired energy loss spectra of the O K-edge (left) and Ni $L_{2,3}$-edge (right). The intensities were normalised at the maximal intensity of the O K-edge. Additionally the spectra were aligned at the O K-edge.

performed. The different spectra were aligned at the maximum of the O K-edge in order to correct for small drifts in the high voltage system and the energy filter. In addition the intensities were normalised at the maximal intensity of the O K-edge. The spectra are shown in figure 7.6. It is evident that the relative intensities of the two edges are different for each of the chosen detector positions.

As these measurements at the G20 with a LaB_6 cathode were successful, further measurements were performed at the F20 with a FEG to get more intensity and a better signal-to-noise ratio (SNR). These measurements are described in the following.

Again a bright field image of the investigated area of the specimen is shown in figure 7.7. A similar experimental setup as for the measurements described above was used. As before, the specimen was tilted out of the [1 1 0] zone axis to obtain a systematic row condition including the $(\bar{1}\,1\,1)$ diffraction spot. The corresponding diffraction pattern is shown in figure 7.8.

The thickness was measured according to the Log-ratio method using a low loss spectrum which is shown in figure 7.9. The obtained thickness was 30 nm and is estimated to lie in an interval of 2 nm around the calculated nominal value. From the FWHM of the zero loss peak the experimental broadening was determined to be 1.5 eV.

The EELS measurements were performed at the detector positions $(\eta, \kappa) = (0.2, 0.3)$, $(0.8, 0.3)$, $(1.2, 0.3)$ and $(1.8, 0.3)$. The SAA, whose effective size back-projected on the objective plane was 200 nm, was used so that the thickness of the investigated

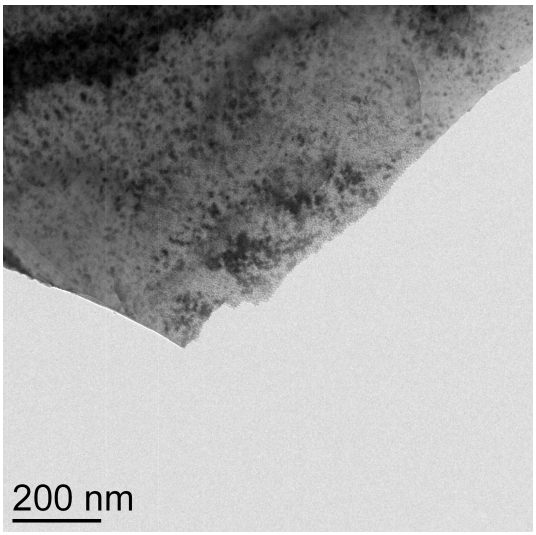

Figure 7.7.: Bright field image of the investigated sample area.

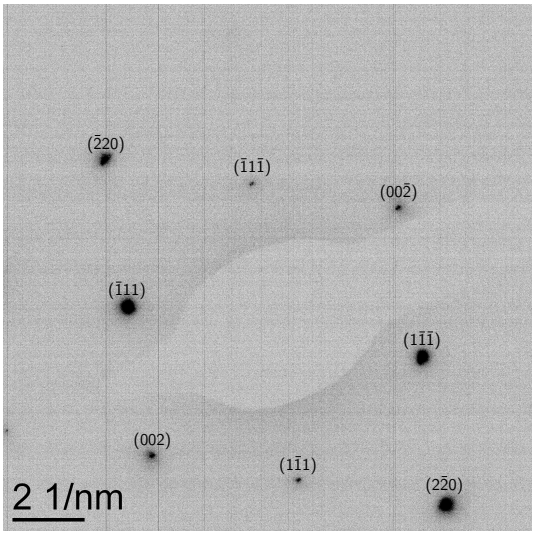

Figure 7.8.: Diffraction pattern of NiO in systematic row condition including the $(\bar{1}\,1\,1)$ diffraction spot. Due to the close proximity to the systematic row, adjacent diffraction spots show up as well.

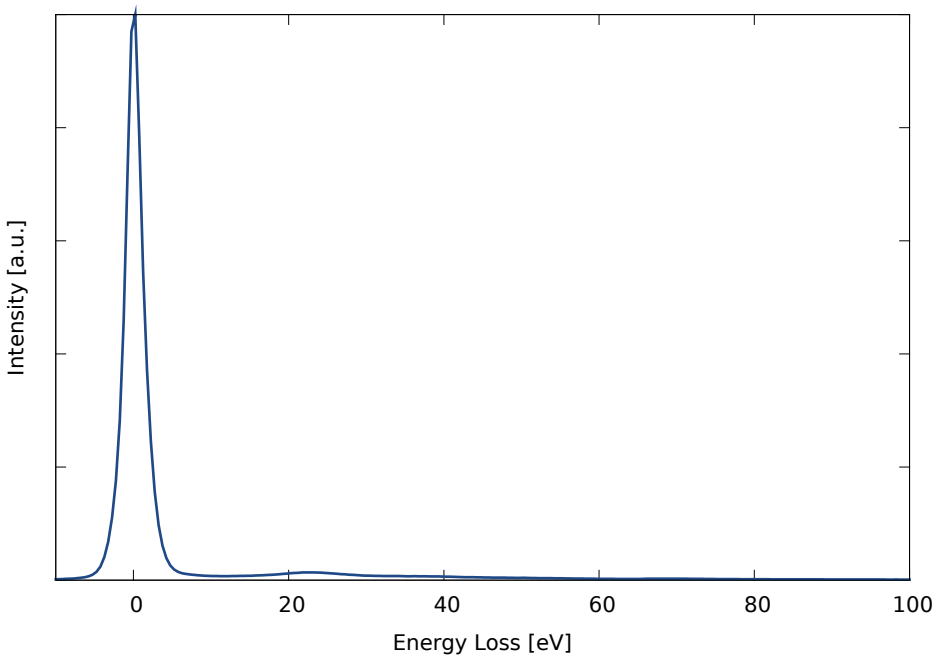

Figure 7.9.: Low loss spectrum of NiO acquired on the F20 at a typical measurement position. Note that the plasmon around 22 eV is barely visible indicating a thin specimen. The Log-ratio method yields a thickness of 30 nm.

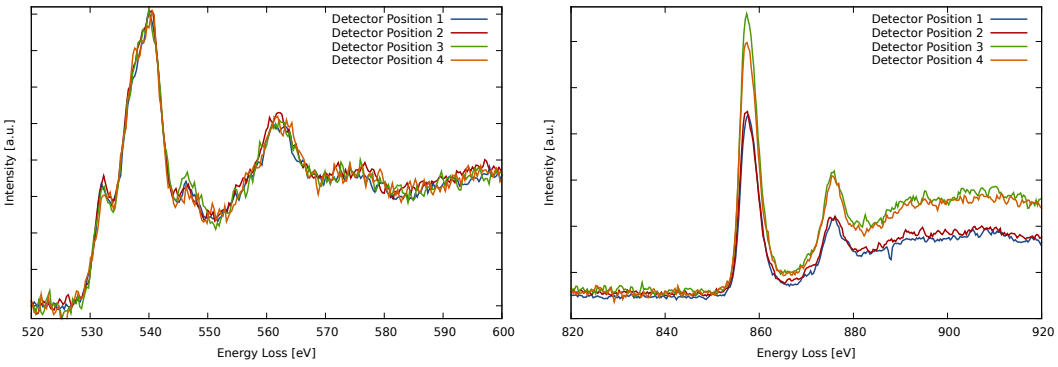

Figure 7.10.: Acquired energy loss spectra of the O K-edge (left) and Ni $L_{2,3}$-edge (right). The intensities were normalised at the maximal intensity of the O K-edge. Additionally the spectra were aligned at the O K-edge.

area did not change too much. A SEA of 3 mm diameter corresponding to a collection semi-angle $\beta = 1.2$ mrad and a dispersion of 0.5 eV per pixel were chosen. The acquisition time was 180 s for each measurement. A background subtraction using a power-law fit [54] was performed. The different spectra were again aligned at the maximum of the O K-edge in order to correct for small drifts in the high voltage system and the energy filter. The intensities were normalised at the maximal intensity of the O K-edge. Additionally the spectra were aligned at the O K-edge. The spectra are shown in figure 7.10. Unfortunately the specimen drifted away after measuring at the detector positions $(\eta, \kappa) = (1.2, 0.3)$ and $(1.8, 0.3)$, labelled as positions 3 and 4. Therefore, the measurements at positions 1 and 2 are unusable for comparison as the specimen thickness for this measurements is not known.

7.2. Results

The results of the measurements conducted at the G20 are shown in figures 7.6 and 7.11. The statistical errors were determined by calculating the standard deviations of each measurement in a pre-edge background region using the program Digital Micrograph. Subsequent calculation of the propagation of error yields standard deviations σ of the order of 5%. In addition, systematic errors occur due to the fact that the EELS detector is not point-like but the acquired signal is integrated over the SEA. To estimate the orders of magnitude of these systematic errors when measuring the signal intensities at different detector positions, the behaviour of the DDSC was investigated. This was done by numerically integrating the DFF and the MDFF over the SEA. The result was then compared to the value at the nominal position of the EELS detector. The systematic errors were determined to be very small (of the order of 0.1%) compared to the statistical errors and are therefore neglected in the following. For drawing the error bars $\pm 2\sigma$ was used in order to obtain a confidence interval of 95.4%.

When comparing the experimental values with the simulations, the intensities of the Ni $L_{2,3}$-edge are normalised with respect to the intensity at position 1. The obtained values are marked with the corresponding error bars in figure 7.11. It can be seen that the experiment shows very good agreement with the simulations.

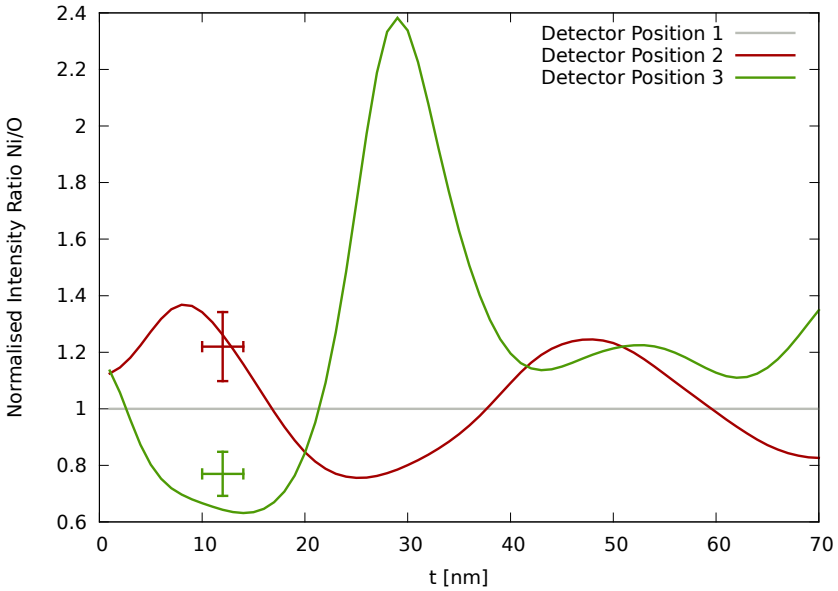

Figure 7.11.: Comparison of the measured relative intensities at different detector positions with simulations. The measured values of the normalised Ni $L_{2,3}$-edge intensities are marked with error bars.

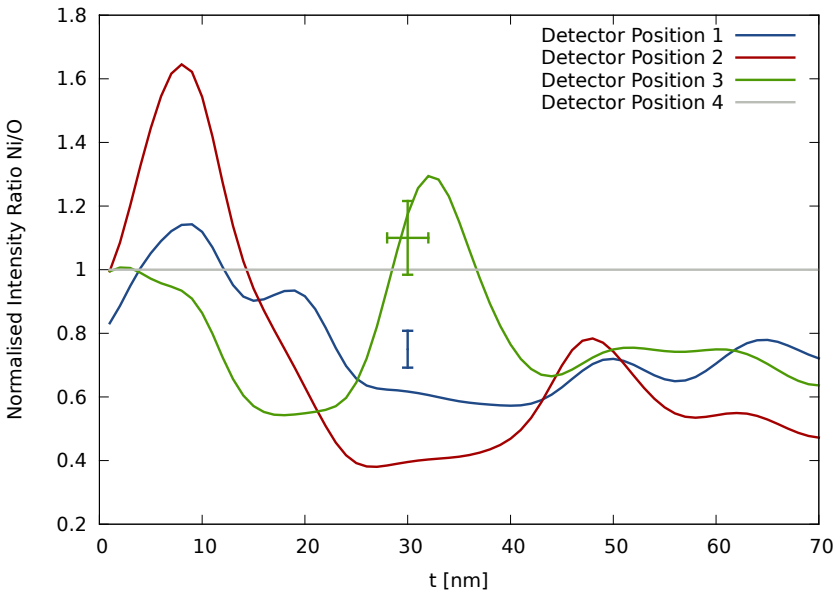

Figure 7.12.: Comparison of the measured relative intensities at different detector positions with simulations. The measured values of the normalised Ni $L_{2,3}$-edge intensities are marked with error bars.

The measured intensity can be described approximately as follows:

$$I(\eta, \kappa, E, atom, \alpha) = p_{mic} \cdot f(E, atom) \cdot g(\eta, \kappa, E, \alpha)\,, \tag{7.1}$$

where p_{mic} are microscopic parameters, $f(E, atom)$ are the factors $f(E)$ of equation (5.46) and $g(\eta, \kappa, E, \alpha)$ incorporates all the Bloch-wave related factors and the factor $(\boldsymbol{Q} \cdot \boldsymbol{Q}')/(Q^2 Q'^2)$ of equation (5.42). E is the energy loss of the corresponding inelastic scattering process, α depends on sample thickness, orientation and other parameters while η, κ define the detector position. When calculating the ratio of the Ni signal and the O signal, the microscopic parameters cancel:

$$\frac{I(\eta, \kappa, E_{Ni}, Ni, \alpha_{Ni})}{I(\eta, \kappa, E_O, O, \alpha_O)} = \frac{f(E_{Ni}, Ni)}{f(E_O, O)} \cdot \frac{g(\eta, \kappa, E_{Ni}, \alpha_{Ni})}{g(\eta, \kappa, E_O, \alpha_O)}\,. \tag{7.2}$$

Furthermore, when normalising the spectra acquired at different positions with the intensities of one specific position of the EELS detector, all the factors $f(E, atom)$ cancel.

$$\begin{aligned}\left(\frac{I(\eta_1, \kappa_1, E_{Ni}, Ni, \alpha_{Ni})}{I(\eta_1, \kappa_1, E_O, O, \alpha_O)}\right) \Bigg/ \left(\frac{I(\eta_2, \kappa_2, E_{Ni}, Ni, \alpha_{Ni})}{I(\eta_2, \kappa_2, E_O, O, \alpha_O)}\right) = \\ = \frac{g(\eta_1, \kappa_1, E_{Ni}, \alpha_{Ni})}{g(\eta_1, \kappa_1, E_O, \alpha_O)} \Bigg/ \frac{g(\eta_2, \kappa_2, E_{Ni}, \alpha_{Ni})}{g(\eta_2, \kappa_2, E_O, \alpha_O)}\,.\end{aligned} \tag{7.3}$$

The results of the measurements performed at the F20 are shown in figures 7.10 and 7.12. The measured intensities are normalised with respect to the intensity at detector position 4. The results with corresponding error bars for the measured intensities and specimen thickness are shown in figure 7.12. As mentioned above, the sample drifted away after measuring at positions 3 and 4. Thus, the specimen thickness for these measurements are not known. Therefore no error bar for the specimen thickness is drawn for the measurements at detector positions 1 and 2. As the results at these two positions are very similar only one of these two measurements is drawn in figure 7.12.

Despite this, the good agreement of experimentally acquired relative signal intensities and the corresponding simulations is evident.

It is notable that, despite the measurements at positions that yield low intensities, no further treatment of the acquired spectra (except background subtraction) was necessary. Especially, no post-processing to obtain spectra out of measured data

using some sort of deconvolution algorithm was used (as it was necessary in [50]).

Some approximations are made in the simulations. For instance the electron waves are supposed to be plane waves but in the TEM the electron beam is slightly converged due to intensity reasons. Further the dipole approximation for the DFF and MDFF is used, see [59]. But despite all this, the experimentally acquired spectra are in very good agreement with the calculations.

Part IV.

Conclusion

8. Summary and Outlook

Two fields in transmission electron microscopy need a detailed description by simulations. These are the calculation of the electronic structure of the sample material and the accurate modelling of the probe–target interaction. Both fields were treated thoroughly in this thesis.

The electronic structure of NiO was calculated using the DFT based simulation package WIEN2k. As NiO is a transition-metal oxide, the description of the exchange-correlation potential is crucial. Therefore, different methods to calculate the exchange-correlation energy were used to calculate the DOS and ELNES spectra of NiO. The results obtained using GGA, LDA+U, two different hybrid functionals (PBE0, B3PW91) and the modified Becke-Johnson potential were compared.

It was shown that in the GGA calculation the fundamental band gap is severely underestimated. Using the LDA+U method gives major improvements compared to GGA but the gap width is still underestimated. Also when the hybrid functionals were used the fundamental band gap was too small. Only when utilizing the modified Becke-Johnson potential the calculated fundamental band gap width is in good agreement with both literature and experiments.

Concerning ELNES, the GGA and LDA+U calculations revealed some differences to the experimentally acquired O K-edge spectra. Using hybrid exchange-correlation functionals improved the calculated spectra only slightly. However, when the modified Becke-Johnson potential was used, the calculated spectrum fit the experimental data very well. Different methods to calculate the exchange-correlation energy revealed only minor differences in the Ni $L_{2,3}$-edge. This suggests that the Ni-DOS calculated with WIEN2k is not entirely correct.

Additionally, low voltage VEELS was performed to obtain optical properties of NiO by means of Kramers-Kronig analysis. Furthermore, the value of the optical band gap was determined from the low voltage spectrum. The results show very good agreement with the calculated optical band gap using hybrid functionals and the

modified Becke-Johnson potential, as well as measurements, both reported previously in literature.

To sum it up, choosing an appropriate calculation method for the exchange-correlation energy is crucial for the results of the calculation. The modified Becke-Johnson potential turned out to be the best choice for the transition-metal oxide NiO.

To investigate the effects of probe–target interaction a simulation program based on a combination of the Bloch-wave formalism for elastic scattering and the mixed dynamic form factor for inealstic scattering was applied. The relative signal intensities of the Oxygen and Nickel signal for different positions of the EELS detector were calculated. The results were compared to site selective energy loss data obtained by means of ELCE-experiments.

The measurement positions a certain distance away from the diffraction spots yield spectra with low intensity. But despite this fact no further treatment of the spectra except background subtraction was necessary. Furthermore, some approximations were made when performing the calculations. Keeping this in mind, the acquired spectra show a very good agreement to the simulations.

All in all, owing to powerful simulation software, sophisticated techniques like ELCE are transforming from rather exotic applications to promising methods for analytical transmission electron microscopy.

In this thesis it was shown that new simulation methods can help to explain experimental data which is acquired with unprecedented quality and precision due to a new generation of corrected microscopes. The ab-initio simulation software WIEN2k is capable of calculating the electronic structure but does not take into account elastic scattering of the electron beam in the crystal. In a wide variety of modern analytical techniques elastic scattering is of high importance, however. When investigating the effects of probe–target interaction, the combination of elastic with inelastic scattering is of interest. The program used for this part of the thesis simulates elastic scattering but has only rudimentary support for inelastic scattering. Thus, the aim of future work should be the implementation of an accurate description of inelastic scattering based on WIEN2k data in the utilized simulation software.

List of Abbreviations

ALCHEMI — Atom Location by Channelling Enhanced Microanalysis

APW — Augmented Plane Wave

APW+lo — Augmented Plane Waves + Local Orbitals, see equation (3.28)

B3PW91 — A type of hybrid exchange-correlation functionals

BF — Bright Field

DDSC — Double Differential Scattering Cross-Section

DFF — Dynamic Form Factor

DFT — Density Functional Theory

DOS — Density Of States

EDX — Energy Dispersive X-Ray Analysis

EELS — Electron Energy Loss Spectrometry

ELCE — Energy Loss by Channelled Electrons

ELNES — Energy Loss Near Edge Structure

EMCD — Energy-Loss Magnetic Chiral Dichroism

F20 — FEI TECNAI G^2 F20 Transmission Electron Microscope

FP-LAPW — Full Potential Linearized Augmented Plane Wave

FWHM — Full Width at Half Maximum

G20 — FEI TECNAI G^2 20 Transmission Electron Microscope

GGA — Generalized Gradient Approximation

HF — Hartree-Fock

LAPW — Linearized Augmented Plane Wave

LDA — Local Density Approximation

LDA+U — LDA including the description of Coulomb interaction of two electrons with different spins

LO — Local Orbitals, see equation (3.26)

mBJ — Modified Becke-Johnson potential

mBJLDA — Modified Becke-Johnson potential used together with LDA

MDFF — Mixed Dynamic Form Factor

PBE — A commonly used variant of GGA described by Perdew, Burke and Ernzerhof

PBE0 — A type of hybrid exchange-correlation functionals

SAA — Selected Area Aperture

SCF — Self-Consistent Field

SEA — Spectrometer Entrance Aperture

SIC — Self Interaction Correction

SNR — Signal-To-Noise Ratio

TEM — Transmission Electron Microscope or Transmission Electron Microscopy depending on context

VEELS — Valence Electron Energy Loss Spectrometry

XML — Extensible Markup Language

ZLP — Zero Loss Peak

List of Figures

List of Tables

Bibliography

[1] Blaha, P., Schwarz, K., Madsen, G.K.H., Kvasnicka, D., Luitz, J. *WIEN2k, An Augmented Plane Wave + Local Orbitals Program for Calculating Crystal Properties.* Technische Universität Wien, Austria, 2001. ISBN 3-9501031-1-2.

[2] Tran, F., Blaha, P., Schwarz, K., Novák, P. *Hybrid exchange-correlation energy functionals for strongly correlated electrons: Applications to transition-metal monoxides.* Phys. Rev. B, 74(15), 155108, 2006.

[3] Tran, F., Blaha, P. *Accurate Band Gaps of Semiconductors and Insulators with a Semilocal Exchange-Correlation Potential.* Phys. Rev. Lett., 102(22), 226401, 2009.

[4] Williams, D.B., Carter, C.B. *Transmission Electron Microscopy.* Springer Science+Business Media, 2009. ISBN 978-0-387-76501-3.

[5] Dwyer, C., Etheridge, J. *Scattering of Å-scale electron probes in silicon.* Ultramicroscopy, 96(3-4), 343–360, 2003. ISSN 0304-3991.

[6] Taftø, J., Krivanek, O.L. *Site-Specific Valence Determination by Electron Energy-Loss Spectroscopy.* Phys. Rev. Lett., 48(8), 560–563, 1982.

[7] Taftø, J., Spence, J.C.H. *Crystal Site Location of Iron and Trace Elements in a Magnesium-Iron Olivine by a New Crystallographic Technique.* Science, 218(4567), 49–51, 1982. doi:10.1126/science.218.4567.49.

[8] Schattschneider, P., Rubino, S., Hebert, C., Rusz, J., Kunes, J., Novák, P., Carlino, E., Fabrizioli, M., Panaccione, G., Rossi, G. *Detection of magnetic circular dichroism using a transmission electron microscope.* Nature, 441(7092), 486–488, 2006. ISSN 0028-0836.

[9] Roth, W.L. *Magnetic Structures of MnO, FeO, CoO, and NiO.* Phys. Rev., 110(6), 1333–1341, 1958.

[10] Roth, W.L. *Neutron and Optical Studies of Domains in NiO.* J. Appl. Phys., 31(11), 2000–2011, 1960. doi:10.1063/1.1735486.

[11] Villars, P., Calvert, L., editors. *Pearson's Handbook of Crystallographic Data for Intermetallic Phases.* ASM International, 1996. ISBN 0-87170-416-1.

[12] Fromme, B. *d-d Excitations in Transition-Metal Oxides*, volume 170 of *Springer Tracts in modern physics.* Springer-Verlag Berlin Heidelberg New York, 2001. ISBN 3-540-41051-1.

[13] Schuler, T.M., Ederer, D.L., Itza-Ortiz, S., Woods, G.T., Callcott, T.A., Woicik, J.C. *Character of the insulating state in NiO: A mixture of charge-transfer and Mott-Hubbard character.* Phys. Rev. B, 71(11), 115113, 2005.

[14] Hohenberg, P., Kohn, W. *Inhomogeneous Electron Gas.* Phys. Rev., 136(3B), B864–B871, 1964.

[15] Kohn, W., Sham, L.J. *Self-Consistent Equations Including Exchange and Correlation Effects.* Phys. Rev., 140(4A), A1133–A1138, 1965.

[16] Singh, D.J., Nordstrom, L., editors. *Planewaves, Pseudopotentials, and the LAPW Method.* Springer, second edition, 2006. ISBN 0-387-28780-9.

[17] Cottenier, S. *Density Functional Theory and the family of (L)APW-methods: a step-by-step introduction.* Instituut voor Kern- en Stralingsfysica, K.U. Leuven, Belgium, 2002. ISBN 90-807215-1-4.

[18] Perdew, J.P., Burke, K., Ernzerhof, M. *Generalized Gradient Approximation Made Simple.* Phys. Rev. Lett., 77(18), 3865–3868, 1996.

[19] Anisimov, V.I., Solovyev, I.V., Korotin, M.A., Czyzdotyk, M.T., Sawatzky, G.A. *Density-functional theory and NiO photoemission spectra.* Phys. Rev. B, 48(23), 16929–16934, 1993.

[20] Shick, A.B., Liechtenstein, A.I., Pickett, W.E. *Implementation of the LDA+U method using the full-potential linearized augmented plane-wave basis.* Phys. Rev. B, 60(15), 10763–10769, 1999.

[21] Novák, P. *Expression for total energy in LDA+U methods*, 2001.

[22] Ernzerhof, M., Scuseria, G.E. *Assessment of the Perdew–Burke–Ernzerhof exchange-correlation functional.* J. Chem. Phys., 110(11), 5029–5036, 1999.

[23] Adamo, C., Barone, V. *Toward reliable density functional methods without adjustable parameters: The PBE0 model.* J. Chem. Phys., 110(13), 6158–6170, 1999.

[24] Becke, A.D. *Density-functional thermochemistry. III. The role of exact exchange.* J. Chem. Phys., 98(7), 5648–5652, 1993.

[25] Becke, A.D. *Density-functional exchange-energy approximation with correct asymptotic behavior.* Phys. Rev. A, 38(6), 3098–3100, 1988.

[26] Perdew, J.P., Chevary, J.A., Vosko, S.H., Jackson, K.A., Pederson, M.R., Singh, D.J., Fiolhais, C. *Atoms, molecules, solids, and surfaces: Applications of the generalized gradient approximation for exchange and correlation.* Phys. Rev. B, 46(11), 6671–6687, 1992.

[27] Perdew, J.P., Chevary, J.A., Vosko, S.H., Jackson, K.A., Pederson, M.R., Singh, D.J., Fiolhais, C. *Erratum: Atoms, molecules, solids, and surfaces: Applications of the generalized gradient approximation for exchange and correlation.* Phys. Rev. B, 48(7), 4978, 1993.

[28] Novák, P., Kuneš, J., Chaput, L., Pickett, W.E. *Exact exchange for correlated electrons.* phys. stat. sol. (b), 243(3), 563–572, 2006. ISSN 1521-3951.

[29] Becke, A.D., Johnson, E.R. *A simple effective potential for exchange.* J. Chem. Phys., 124(22), 221101–4, 2006.

[30] Becke, A.D., Roussel, M.R. *Exchange holes in inhomogeneous systems: A coordinate-space model.* Phys. Rev. A, 39(8), 3761–3767, 1989.

[31] Tran, F., Blaha, P., Schwarz, K. *Band gap calculations with Becke-Johnson exchange potential.* J. Phys.: Condens. Matter, 19(19), 196208, 2007.

[32] Blöchl, P.E., Jepsen, O., Andersen, O.K. *Improved tetrahedron method for Brillouin-zone integrations.* Phys. Rev. B, 49(23), 16223–16233, 1994.

[33] Kittel, C. *Einführung in die Festkörperphysik*. Oldenbourg Verlag, 2006. ISBN 3-486-57723-9.

[34] Jorissen, K. *The ab initio calculation of relativistic electron energy loss spectra*. Ph.D. thesis, Universiteit Antwerpen, 2007.

[35] Nelhiebel, M., Louf, P.H., Schattschneider, P., Blaha, P., Schwarz, K., Jouffrey, B. *Theory of orientation-sensitive near-edge fine-structure core-level spectroscopy*. Phys. Rev. B, 59(20), 12807–12814, 1999.

[36] Keski-Rahkonen, O., Krause, M.O. *Total and partial atomic-level widths*. Atomic Data and Nuclear Data Tables, 14(2), 139–146, 1974. ISSN 0092-640X.

[37] Moreau, P., Boucher, F., Goglio, G., Foy, D., Mauchamp, V., Ouvrard, G. *Electron energy-loss spectra calculations and experiments as a tool for the identification of a lamellar C_3N_4 compound*. Phys. Rev. B, 73(19), 195111, 2006.

[38] Muller, D.A., Singh, D.J., Silcox, J. *Connections between the electron-energy-loss spectra, the local electronic structure, and the physical properties of a material: A study of nickel aluminum alloys*. Phys. Rev. B, 57(14), 8181–8202, 1998.

[39] Hébert, C. *Practical aspects of running the WIEN2k code for electron spectroscopy*. Micron, 38(1), 12–28, 2007. ISSN 0968-4328.

[40] Sawatzky, G.A., Allen, J.W. *Magnitude and Origin of the Band Gap in NiO*. Phys. Rev. Lett., 53(24), 2339–2342, 1984.

[41] Mauchamp, V., Jaouen, M., Schattschneider, P. *Core-hole effect in the one-particle approximation revisited from density functional theory*. Phys. Rev. B, 79(23), 235106, 2009.

[42] Dobysheva, L.V., Potapov, P.L., Schryvers, D. *Electron-energy-loss spectra of NiO*. Phys. Rev. B, 69(18), 184404, 2004.

[43] Cai, T., Han, H., Yu, Y., Gao, T., Du, J., Hao, L. *Study on the ground state of NiO: The LSDA (GGA)+U method*. Physica B: Condensed Matter, 404(1), 89 – 94, 2009. ISSN 0921-4526. doi:10.1016/j.physb.2008.10.009.

[44] Powell, R.J., Spicer, W.E. *Optical Properties of NiO and CoO.* Phys. Rev. B, 2(6), 2182–2193, 1970.

[45] Stöger-Pollach, M. *Optical properties and bandgaps from low loss EELS: Pitfalls and solutions.* Micron, 39(8), 1092–1110, 2008. ISSN 0968-4328.

[46] Stöger-Pollach, M., Franco, H., Schattschneider, P., Lazar, S., Schaffer, B., Grogger, W., Zandbergen, H. *Cerenkov losses: A limit for bandgap determination and Kramers-Kronig analysis.* Micron, 37(5), 396–402, 2006. ISSN 0968-4328.

[47] Stöger-Pollach, M. *Low voltage TEM: Influences on electron energy loss spectrometry experiments.* Micron, 41(6), 577–584, 2010. ISSN 0968-4328.

[48] Spence, J., Taftø, J. *ALCHEMI: a new technique for locating atoms in small crystals.* Journal of Microscopy, 130(Pt 2), 147–154, 1983. ISSN 0022-2720.

[49] Krivanek, O., Disko, M., Taftø, J., Spence, J. *Electron energy loss spectroscopy as a probe of the local atomic environment.* Ultramicroscopy, 9(3), 249–254, 1982. ISSN 0304-3991.

[50] Tatsumi, K., Muto, S. *Local electronic structure analysis by site-selective ELNES using electron channeling and first-principles calculations.* J. Phys.: Condens. Matter, 21(10), 104213, 2009. doi:10.1088/0953-8984/21/10/104213.

[51] Nelhiebel, M. *Effects of crystal orientation and interferometry in electron energy loss spectroscopy.* Ph.D. thesis, École Central Paris, 1999.

[52] Reimer, L. *Transmission Electron Microscopy*, volume 36 of *Springer Series in Optical Sciences.* Springer-Verlag Berlin Heidelberg New York Tokyo, 1984. ISBN 3-540-11794-6.

[53] Schattschneider, P., Hébert, C., Franco, H., Jouffrey, B. *Anisotropic relativistic cross sections for inelastic electron scattering, and the magic angle.* Phys. Rev. B, 72(4), 045142, 2005.

[54] Egerton, R.F. *Electron Energy-Loss Spectroscopy in the Electron Microscope.* Plenum Press New York, second edition, 1996. ISBN 0-306-45223-5.

[55] Löffler, S., Schattschneider, P. *A software package for the simulation of energy-loss magnetic chiral dichroism.* Ultramicroscopy, 110(7), 831–835, 2010. ISSN 0304-3991.

[56] Schattschneider, P., Ennen, I., Löffler, S., Stoger-Pollach, M., Verbeeck, J. *Circular dichroism in the electron microscope: Progress and applications (invited).* J. Appl. Phys., 107(9), 09D311–6, 2010.

[57] Kohl, H., Rose, H. *Theory of Image Formation by Inelastically Scattered Electrons in the Electron Microscope.* In P.W. Hawkes, editor, *Advances in Electronics and Electron Physics*, volume 65 of *Advances in Electronics and Electron Physics*, pages 173 – 227. Academic Press, 1985. doi:10.1016/S0065-2539(08)60878-1.

[58] Findlay, S., Schattschneider, P., Allen, L. *Imaging using inelastically scattered electrons in CTEM and STEM geometry.* Ultramicroscopy, 108(1), 58–67, 2007. ISSN 0304-3991.

[59] Löffler, S., Ennen, I., Tian, F., Schattschneider, P., Jaouen, N. *Breakdown of the dipole approximation in core losses.* Ultramicroscopy, In Press, Uncorrected Proof, 2011. ISSN 0304-3991.